Enhanced ferroelectricity in ultrathin films grown directly on silicon

https://doi.org/10.1038/s41586-020-2208-x

Received: 15 July 2019

Accepted: 27 January 2020

Suraj S. Cheema[1,13]✉, Daewoong Kwon[2,12,13], Nirmaan Shanker[1,2], Roberto dos Reis[3], Shang-Lin Hsu[3,7], Jun Xiao[4], Haigang Zhang[5], Ryan Wagner[5], Adhiraj Datar[1,2], Margaret R. McCarter[6], Claudy R. Serrao[2], Ajay K. Yadav[2], Golnaz Karbasian[2], Cheng-Hsiang Hsu[2], Ava J. Tan[2], Li-Chen Wang[1], Vishal Thakare[1], Xiang Zhang[4], Apurva Mehta[8], Evguenia Karapetrova[9], Rajesh V Chopdekar[10], Padraic Shafer[10], Elke Arenholz[10,11], Chenming Hu[2], Roger Proksch[5], Ramamoorthy Ramesh[1,6], Jim Ciston[3] & Sayeef Salahuddin[2,7]✉

Ultrathin ferroelectric materials could potentially enable low-power logic and nonvolatile memories[1,2]. As ferroelectric materials are made thinner, however, the ferroelectricity is usually suppressed. Size effects in ferroelectrics have been thoroughly investigated in perovskite oxides—the archetypal ferroelectric system[3]. Perovskites, however, have so far proved unsuitable for thickness scaling and integration with modern semiconductor processes[4]. Here we report ferroelectricity in ultrathin doped hafnium oxide (HfO_2), a fluorite-structure oxide grown by atomic layer deposition on silicon. We demonstrate the persistence of inversion symmetry breaking and spontaneous, switchable polarization down to a thickness of one nanometre. Our results indicate not only the absence of a ferroelectric critical thickness but also enhanced polar distortions as film thickness is reduced, unlike in perovskite ferroelectrics. This approach to enhancing ferroelectricity in ultrathin layers could provide a route towards polarization-driven memories and ferroelectric-based advanced transistors. This work shifts the search for the fundamental limits of ferroelectricity to simpler transition-metal oxide systems—that is, from perovskite-derived complex oxides to fluorite-structure binary oxides—in which 'reverse' size effects counterintuitively stabilize polar symmetry in the ultrathin regime.

Ferroelectric materials exhibit stable states of collectively ordered electrical dipoles whose polarization can be reversed under an applied electric field[5]. Consequently, ultrathin ferroelectrics are of great technological interest for high-density electronics, particularly field-effect transistors and non-volatile memories[2]. However, ferroelectricity is typically suppressed at the scale of a few nanometres in the ubiquitous perovskite oxides[6]. First-principles calculations predict six unit cells to be the critical thickness in perovskite ferroelectrics[1] owing to incomplete screening of depolarization fields[3]. Atomic-scale ferroelectricity in perovskites often fails to demonstrate polarization switching[7,8], which is crucial for applications. Furthermore, attempts to synthesize ferroelectric perovskite films on silicon[9,10] are impeded by chemical incompatibility[4,11] and the high temperatures required for epitaxial growth. Since the discovery of ferroelectricity in HfO_2-based thin films in 2011[12], fluorite-structure binary oxides (fluorites) have attracted considerable interest[13] because they enable low-temperature synthesis and conformal growth in three-dimensional structures on silicon[14,15], thereby overcoming many of the issues that restrict its perovskite counterparts in terms of complementary metal-oxide-semiconductor (CMOS) compatibility and thickness scaling[16]. Considering the extensive implications for future computing[2,17,18], achieving ferroelectricity in sub-2-nm-thick doped-HfO_2 is highly desirable for realizing ultra-scaled CMOS-compatible ferroelectric-based devices beyond the 5 nm technology node[19].

Here we demonstrate ferroelectricity in ultrathin (1 nm thick) $Hf_{0.8}Zr_{0.2}O_2$ (HZO), grown by low-temperature atomic layer deposition (ALD) on silicon. Second harmonic generation and advanced scanning probe techniques establish the presence of inversion symmetry breaking and switchable electric polarization, respectively. Not only is ferroelectricity stabilized in ultrathin HZO, but spectroscopic and diffraction signatures of its fluorite-structure symmetry also indicate enhanced polar distortion in the ultrathin regime. Such size effects in this fluorite-structure system do not occur in its perovskite counterparts[6], which can be understood from symmetry considerations. In

---

[1]Department of Materials Science and Engineering, University of California, Berkeley, CA, USA. [2]Department of Electrical Engineering and Computer Sciences, University of California, Berkeley, CA, USA. [3]National Center for Electron Microscopy, Molecular Foundry, Lawrence Berkeley National Laboratory, Berkeley, CA, USA. [4]Nanoscale Science and Engineering Center, University of California, Berkeley, CA, USA. [5]Asylum Research, Oxford Instruments, Santa Barbara, CA, USA. [6]Department of Physics, University of California, Berkeley, Berkeley, CA, USA. [7]Materials Sciences Division, Lawrence Berkeley National Laboratory, Berkeley, CA, USA. [8]Stanford Synchrotron Radiation Lightsource, SLAC National Accelerator Laboratory, Menlo Park, CA, USA. [9]Advanced Photon Source, Argonne National Laboratory, Argonne, IL, USA. [10]Advanced Light Source, Lawrence Berkeley National Laboratory, Berkeley, CA, USA. [11]Cornell High Energy Synchrotron Source, Cornell University, Ithaca, NY, USA. [12]Present address: Department of Electrical Engineering, Inha University, Incheon, South Korea. [13]These authors contributed equally: Suraj S. Cheema, Daewoong Kwon. ✉e-mail: s.cheema@berkeley.edu; sayeef@berkeley.edu

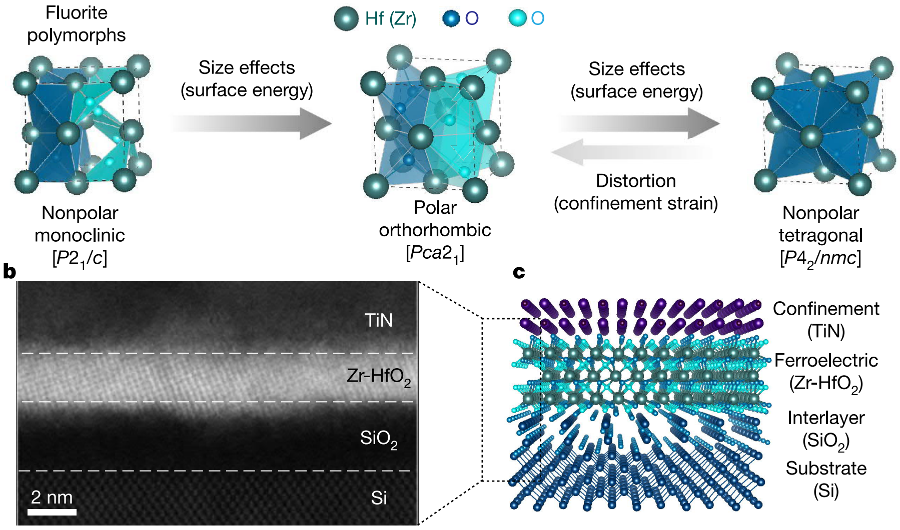

Fig. 1 | Size effects in fluorite-structure ferroelectrics. a, In fluorite-structure ferroelectrics, the polar distortion present in the orthorhombic phase can be represented as the centre anion displacement (cyan) with respect to its surrounding cation tetrahedron (represented by cyan arrow); in the nonpolar tetragonal phase, the oxygen atom (blue) lies in the polyhedral centre of the tetrahedron. The evolution of the bulk-stable monoclinic polymorph to the high-symmetry tetragonal and polar orthorhombic phases in the fluorite-structure structure illustrates the role of size effects – surface energies favour higher symmetry – and confinement strain – distortions favour lower symmetry – on stabilizing inversion asymmetry. In fluorite-structures, the noncentrosymmetric O-phase is higher symmetry relative to the bulk-stable centrosymmetric M-phase. Consequently, both intrinsic (surface energy) and extrinsic (confinement strain) mechanisms can favour ultrathin inversion symmetry breaking in fluorite-structures, in stark contrast to size effect trends perovskites (Extended Data Fig. 1). **b**, Cross-sectional ADF STEM image of 20-cycle (about 1.8 nm) HZO, demonstrating ultrathin HZO films on silicon via low-temperature ALD. The Si substrate is oriented along the [110] zone axis. **c**, Schematic heterostructure investigated in this work, detailing the ultrathin ferroelectric HZO layer deposited on Si/SiO$_2$, and the capping metal layer employed to impart confinement strain during post-deposition rapid thermal annealing (Methods).

classical perovskites, surface-energy-driven size effects at reduced dimensions favour the high-symmetry paraelectric phase (cubic) over the low-symmetry ferroelectric phase (tetragonal)[20]. Conversely, in fluorites, the noncentrosymmetric phase (orthorhombic $Pca2_1$, O-phase) is higher-symmetry relative to the bulk-stable centrosymmetric phase ($P2_1/c$, M-phase)[21]. Consequently, surface energies can promote (destabilize) inversion symmetry breaking in fluorite (perovskite) ferroelectrics in the two-dimensional limit[21,22]. Owing to this size-induced noncentrosymmetry—that is, 'reverse' size effects (Fig. 1a, Extended Data Fig. 1)—HZO presents a promising model system in which to explore the ultrathin limits of ferroelectricity.

Thin films of HZO are grown using ALD down to ten cycles on oxidized silicon at 250 °C. For reference, approximately 11 ALD cycles correspond to 1 nm thickness, as confirmed by X-ray reflectivity (XRR, Extended Data Fig. 2) and transmission electron microscopy (TEM, Extended Data Fig. 3). Subsequently, HZO films are capped by a metal and subjected to rapid thermal annealing—henceforth referred to as confinement strain (Fig. 1c)—to impart anisotropic thermal stresses. Confinement strain has been reported to help distort the high-symmetry tetragonal fluorite-structure polymorph ($P4_2/nmc$, T-phase) into the polar O-phase[13] (Fig. 1a). For confined ultrathin HZO films, X-ray diffraction analysis indicates a highly oriented noncentrosymmetric structure in contrast to polycrystalline thicker films (Extended Data Fig. 4). Inversion symmetry breaking in 10 cycle (about 1 nm) HZO films is confirmed by the presence of second harmonic generation (SHG) (Extended Data Fig. 5), previously employed to demonstrate ferroelectricity in a two-dimensional material[23].

Beyond inversion asymmetry, ferroelectricity also requires electrical switching between polarization states. Resonance-enhanced piezoresponse force microscopy (PFM) demonstrates bistable switching in Si/SiO$_2$/HZO heterostructures (Fig. 2a). PFM phase images on ten-cycle HZO films (Fig. 2d) show well defined regions of 180° phase contrast—corresponding to remanent polarization states (Fig. 2b)—that can be rewritten in a non-volatile fashion. Notably, unpoled regions demonstrate the same phase contrast as positively poled regions (Fig. 2d), indicating that ultrathin HZO exhibits spontaneous polarization. In previous studies, field cycling is often required to 'wake up' the ferroelectricity in HfO$_2$-based fluorites, which is attributed to a field-induced nonpolar-polar phase transition[13]. Here, atomic-scale thickness in tandem with mechanical confinement enhances the polar phase stability to exhibit spontaneous polarization, eliminating one of the most critical issues plaguing fluorite-structure ferroelectrics[16]. Rapid thermal annealing alone is insufficient for ferroelectricity; regions of HZO annealed without a metal capping layer do not exhibit ferroelectric signatures (Extended Data Fig. 6). This highlights the critical role of ultrathin confinement, and the strains imposed by such layering, on stabilizing the polar O-phase in ultrathin fluorite-structure films.

Along with phase contrast imaging, local PFM switching spectroscopy further confirms the robust ferroelectricity in ten-cycle HZO films, as demonstrated by 180° phase hysteresis and its butterfly-shape amplitude (d_{33}) loops (Fig. 2e). PFM spectroscopy was performed on metal electrodes to eliminate electrostatic artefacts from the tip[24] and potential electromechanical contributions (Methods). In addition, careful monitoring of topography was performed during poling (Extended Data Fig. 7a) to detect the possibility of any electrochemical and electromechanical artefacts. Time-dependent PFM imaging (Extended Data Fig. 7b) on ten-cycle HZO illustrates polarization patterns sustained for at least 24 h; such long-term retention suggests that the PFM contrast is due to ferroelectric behaviour and not due to shorter-scale spurious effects often attributed to amorphous hafnia[25]. Furthermore, alternating voltage (V_{ac})-dependent piezoresponse loops (Extended Data Fig. 7c) rule out electrostatic artefacts from charging[25]. Moving beyond the standard PFM optical beam detection method, interferometric displacement sensor (IDS) PFM measurements (Extended Data Fig. 7d) definitively demonstrate the ferroelectric origin of switching spectroscopy hysteresis in ten-cycle HZO. The recently developed IDS

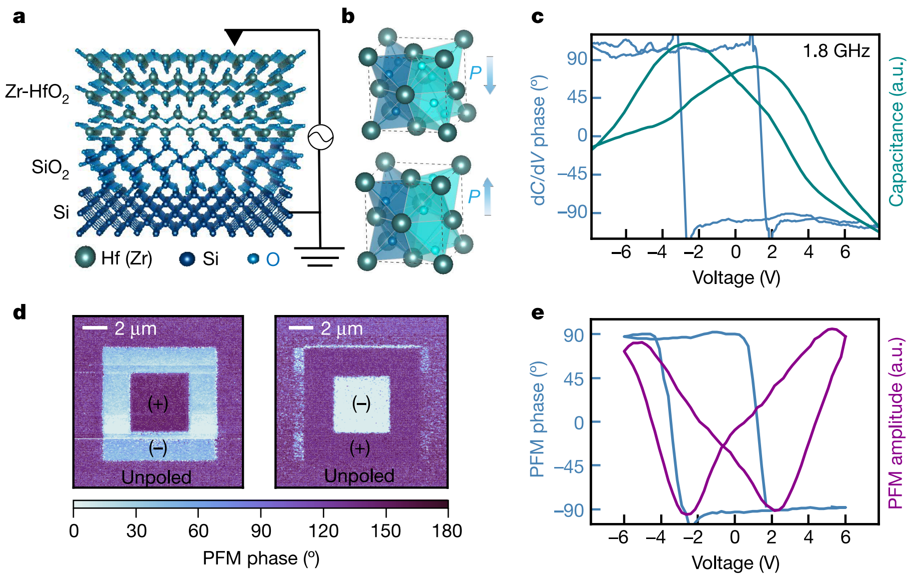

Fig. 2 | Electric polarization switching in ultrathin HZO. a, Schematic of the Si/SiO$_2$ (2 nm)/HZO (1 nm) heterostructure investigated by scanning probe imaging. **b**, Schematic of the HZO unit cell in the ferroelectric orthorhombic structure ($Pca2_1$). The different-coloured oxygen atoms represent the displaced oxygen atoms (cyan) and the centrosymmetric oxygen atoms (blue) within the surrounding cation tetrahedron. The blue arrows labelled P denote the polarization directions corresponding to the acentric oxygen atomic displacements. **c**, Microwave-frequency SCM spectroscopy for a ten-cycle HZO film. The presence of butterfly-shaped C–V conclusively demonstrates ferroelectricity in ultrathin HZO, enabled by the high-frequency detection of differential capacitance (Methods). Microwave dC/dV measurements on multiple regions of ten-cycle HZO demonstrate the robust ferroelectric behaviour (Extended Data Fig. 8). **d**, Phase-contrast PFM images demonstrating stable, bipolar, remanent polarization states that can be overwritten into the opposite polarization state for a ten-cycle HZO film. We note that the unpoled outer perimeter matches phase contrast with the positively poled regime regardless of the poling-polarity sequence; this indicates that ultrathin HZO exhibits spontaneous polarization without requiring 'wake-up' effects to become ferroelectric. Time-dependent PFM imaging further demonstrates the robust ferroelectric contrast (Extended Data Fig. 7). **e**, Phase and amplitude switching spectroscopy loops for a ten-cycle HZO film, demonstrating ferroelectric-like hysteresis. Interferometry-based IDS PFM hysteresis loops confirm that the origin of switching spectroscopy hysteresis is free of artefacts (Extended Data Fig. 7) and switching-spectroscopy measurements demonstrating the critical role of confinement during phase annealing for stabilizing the polar phase in ultrathin HZO (Extended Data Fig. 6).

technique[26] eliminates the long-range electrostatics and cantilever resonance artefacts that obfuscate typical voltage-modulated PFM. Contact IDS measurements demonstrate 180° phase hysteresis and butterfly-shaped d_{33}, which is indicative of ferroelectric behaviour free of electrostatic contributions[26]. A lack of electrostatically driven hysteresis is confirmed by off-surface measurements (Extended Data Fig. 7d). Along with IDS, scanning capacitance microscopy (SCM) provides another advanced scanning probe technique with which to probe ferroelectricity in ultrathin HZO. SCM differential capacitance spectroscopy on ten-cycle HZO demonstrates butterfly-shaped capacitance–voltage (C–V) hysteresis (Fig. 2c, Extended Data Fig. 8). The microwave-frequency detection in SCM (Methods) mitigates the leakage currents that prevent typical bulk electrical characterization of ultrathin ferroelectrics, and provides conclusive evidence of ferroelectric polarization switching.

To examine the structural and electronic origins of ferroelectricity in HZO, we employ grazing-incidence X-ray diffraction (GI-XRD) and X-ray absorption spectroscopy (XAS) (Fig. 3). GI-XRD alone cannot unambiguously distinguish between certain fluorite-structure polymorphs in ultrathin HZO; as a complement to diffraction, XAS provides spectroscopic signatures of the polar O-phase and nonpolar T-phase. In particular, the T-phase nonpolar distortion (D_{4h}, fourfold prismatic symmetry) from regular tetrahedral to fluorite-structure symmetry does not split the degenerate e orbitals ($d_{x^2-y^2}$, $d_{3z^2-r^2}$). Meanwhile, the O-phase polar rhombic pyramidal distortion (C_{2v}, twofold pyramidal symmetry) does split the e manifold, providing a symmetry-specific spectroscopic marker (Extended Data Fig. 9a,b). Owing to the d^0 electronic configuration present in Hf^{4+} (Zr^{4+}), spectral weight from oxygen K-edge XAS can be attributed solely to crystal field effects, providing additional insights into the degree of structural distortion. The spectral weight of the symmetry-split e regimes (Extended Data Fig. 9c) and pre-edge regime (Extended Data Fig. 9e) increases with decreasing thickness, indicative of more pronounced rhombic distortion and divergence from isotropic nearest-neighbour oxygen polyhedral coordination (Extended Data Fig. 9d), respectively. These spectral weight trends provide further evidence of ultrathin-enhanced distortions. In conjunction with XAS, X-ray linear dichroism (XLD) can also probe structural distortions owing to its sensitivity to orbital asymmetry. Nanospectroscopy via soft X-ray photoemission electron microscopy (PEEM) illustrates spatially resolved XLD contrast at 535 eV (Extended Data Fig. 9f), corresponding to the e-split rhombic distortion regime. This suggests that XLD at the O K edge is indeed sensitive to polar features in ultrathin HZO. Shifting to sample-averaged XLD at the Zr M_2 edge, the orbital polarization is found to increase from the thick (100-cycle) to ultrathin (ten-cycle) regime (Fig. 3c), indicative of increased oxygen polyhedral distortion (Fig. 3d) consistent with ultrathin-enhanced ferroelectricity.

Remarkably, we also observe the emergence of crystallographic texturing of HZO films in the ultrathin regime (Fig. 1b, 3e). We note that many of the reflections in 100-cycle HZO, including the dominant (111), are absent in the GI-XRD spectra below 25 cycles owing to the geometric limitations of one-dimensional spectra (unable to detect all the reflections present in highly oriented films) (Methods). Tilted-geometry (φ–χ) diffraction (that is, pole figures) are required to access these oriented reflections at specific points, rather than polycrystalline-like rings, in reciprocal space. The spot-like patterns present in pole figures about the (111) reflections (Extended Data Fig. 4b) confirm the high degree of texturing in ultrathin HZO. Interestingly, this texturing

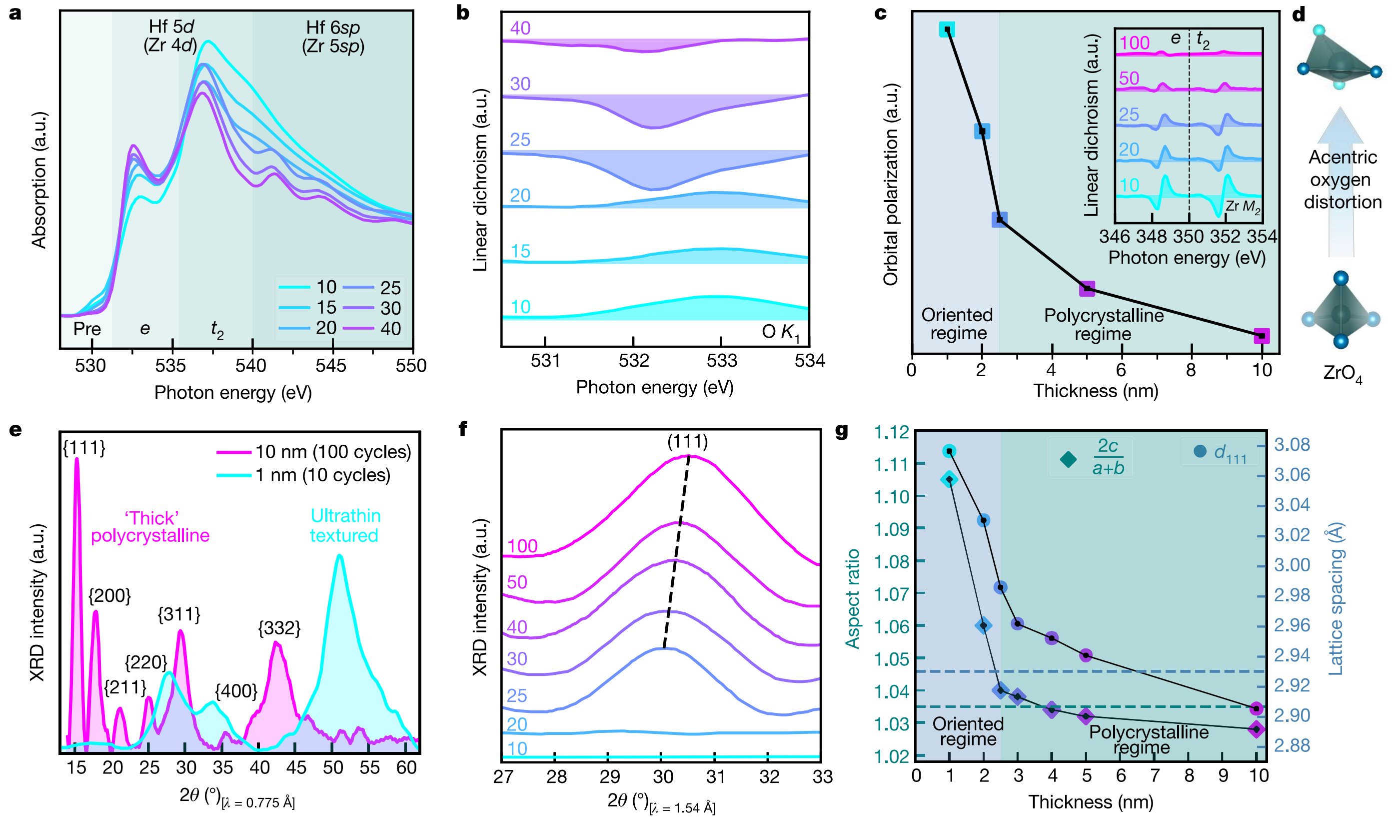

Fig. 3 | Emergence of 'reverse' size effects in ultrathin HZO. a, Thickness-dependent XAS at the O K edge; spectral weight XAS trends indicate enhanced polyhedral disorder and tetrahedral and rhombic distortions in ultrathin films, illustrated by the crystal field splitting diagram for the fluorite-structure structural polymorphs and symmetry-specific XAS simulations (Extended Data Fig. 9a, b). The e and t_2 d-electron energy manifolds are set by the fluorite-structure tetrahedral symmetry (Extended Data Fig. 9a). **b**, Thickness-dependent XLD at the O K edge; the orbital polarization inversion below 25 cycles corresponds to the onset of highly oriented ultrathin films. **c**, Thickness-dependent orbital polarization and XLD (inset) at the Zr M_2 edge. The orbital polarization trend indicates ultrathin-enhanced ZrO_4 tetrahedral distortion, schematically represented in **d** by acentric oxygen atomic displacement (cyan atoms). **e**, Synchrotron GI-XRD demonstrating the emergence of highly oriented ultrathin films, consistent with ADF-STEM (Fig. 1b) and pole figure analysis of ultrathin HZO (Extended Data Fig. 4b). **f**, Thickness-dependent GI-XRD around the polar orthorhombic (111) reflection, demonstrating a systematic shift in $2\theta_{111}$ with thickness, and highlighting the limitation of GI-XRD geometry to detect the (111)-reflection below 25 cycles as the film becomes highly oriented (Extended Data Fig. 4). **g**, Thickness-dependent d_{111} lattice spacing and $2c/(a+b)$ structural aspect ratio, suggesting amplified polarization in the ultrathin limit, especially below 25 cycles. Dashed lines denote reported d_{111} and aspect ratio values for thicker ferroelectric HZO films. Aspect ratio values are extracted from the symmetry-split {200} planes (Methods).

happens despite local nanocrystalline regions observed in TEM for ultrathin films (for example, 15-cycle HZO in Extended Data Fig. 3d). Coinciding with the onset of texturing, the microstructural evolution below 25-cycle HZO manifests spectroscopically as inverted orbital polarization at the e manifold (Fig. 3b), suggesting flipped polar-distortion-split e levels ($d_{x^2-y^2}$ and $d_{3z^2-r^2}$). This indicates that sub-25-cycle ultrathin films enter a new electronic structure concurrently as the crystalline structure orders. Therefore, confinement strain in atomic-scale fluorite films could provide a route to tailor electronic structure and engineer polarization at the orbital level[27], akin to epitaxial strain in perovskite films.

The onset of highly ordered films also coincides with sharp rises in structural markers of distortion (Fig. 3g). The degree of rhombic distortion is captured by the lattice spacing d_{111}; accordingly, d_{111} is tied to macroscopic polarization in HZO[28,29]. We observe increasing d_{111} with decreasing thickness (Fig. 3g), as previously reported in epitaxial HZO films grown by pulsed laser deposition[28,29], consistent with ultrathin-enhanced ferroelectricity. Notably, our low-temperature ALD-grown films on silicon can induce similar structurally induced phenomena observed in high-temperature pulsed-laser-deposition-grown epitaxial films on perovskite templates and extended to an even thinner limit. Furthermore, the d_{111} bifurcation below 25 cycles suggests a link between texturing and amplified distortion in the ultrathin regime. Another crystallographic signature, orthorhombic aspect ratio ($2c/a+b$), also indicates enhanced distortions in the ultrathin regime (Fig. 3g). Fluorite-structure orthorhombicity[13] is akin to perovskite tetragonality[30] (c/a); these ratios serve as structural barometers of macroscopic polarization. The orthorhombic distortion present in ten-cycle HZO far exceeds any reported values for HfO_2-ZrO_2 polymorphs[13]: we find >10% aspect asymmetry, whereas 3–4% is typically reported for fluorite-structure ferroelectrics, consistent with our thicker films (Fig. 3g). Correspondingly, the tetrahedral and rhombic crystal field splitting energies in ultrathin films surpass expected polar fluorite-structure values by 1.3 eV and 700 meV, respectively (Extended Data Fig. 9g). Such colossal structural splittings are well beyond the reported limits of epitaxial strain in perovskite films[27]. Therefore, although prohibitive tunnel currents prevent accurate quantification of polarization from traditional polarization–voltage measurements, multiple structural gauges of polarization indicate substantial enhancement in the ultrathin limit.

In summary, several techniques self-consistently demonstrate robust ferroelectricity in HZO films of thickness down to 1 nm (Extended Data Fig. 2, 3), synthesized by low-temperature ALD on silicon. Remarkably, these experiments indicate that polar distortions are amplified in the ultrathin limit; diffraction markers (d_{111} lattice spacing, structural aspect ratio) and spectroscopic signatures (orbital polarization, crystal field splitting) all demonstrate ultrathin enhancement. Such 'reverse' size effects oppose conventional perovskite ferroelectric trends[6]. Previous works on polycrystalline doped HfO_2[31–33] have explained thickness-dependent polarization trends based on the volume fraction of the ferroelectric O-phase. However, our observations are more consistent with studies of pseudo-epitaxial HZO films grown on perovskite templates[28,29] in that we also observe substantial orientation in the ultrathin regime and enhancement of ferroelectricity with decreasing thickness. Importantly, our work demonstrates that this enhancement persists down to at least two fluorite-structure unit cell thickness, overcoming the deleterious depolarization field effects that would otherwise dominate a prototypical perovskite-structure ferroelectric in this ultrathin regime[1,34]. Further studies should explore how the current understanding of film synthesis, phase competition and polar distortion in HZO developed for thicker films (>5 nm)[35] evolves in the ultrathin regime (<2 nm). Our results indicate that harnessing confinement strain to amplify atomic displacements in ultrathin films provides a route towards enhancing electric polarization at the nanoscale beyond epitaxial strain[36,37], akin to strain gradients in flexoelectricity[38,39]. From a technological perspective, direct monolithic integration of ultrathin doped HfO_2 on Si/SiO_2 paves the way for polarization-driven low-power memories (Extended Data Fig. 10) and ultra-scaled ferroelectrics-based transistors[40,41].

1. Junquera, J. & Ghosez, P. Critical thickness for ferroelectricity in perovskite ultrathin films. *Nature* **422**, 506–509 (2003).
2. Mikolajick, T., Slesazeck, S., Park, M. & Schroeder, U. Ferroelectric hafnium oxide for ferroelectric random-access memories and ferroelectric field-effect transistors. *MRS Bull*. **43**, 340–346 (2018).
3. Dawber, M., Rabe, K. M. & Scott, J. F. Physics of thin-film ferroelectric oxides. *Rev. Mod. Phys*. **77**, 1083–1130 (2005).
4. Schlom, D. G., Guha, S. & Datta, S. Gate oxides beyond SiO_2. *MRS Bull*. **33**, 1017–1025 (2008).
5. Lines, M. E. & Glass, A. M. *Principles and Applications of Ferroelectrics and Related Materials* (Oxford Univ. Press, 1977).
6. Ahn, C., Rabe, K. & Triscone, J. Ferroelectricity at the nanoscale: local polarization in oxide thin films and heterostructures. *Science* **303**, 488–491 (2004).
7. Fong, D. D. et al. Ferroelectricity in ultrathin perovskite films. *Science* **304**, 1650–1653 (2004).
8. Tenne, D. A. et al. Probing nanoscale ferroelectricity by ultraviolet Raman spectroscopy. *Science* **313**, 1614–1616 (2006).
9. Warusawithana, M. P. et al. A ferroelectric oxide made directly on silicon. *Science* **324**, 367–370 (2009).
10. Dubourdieu, C. et al. Switching of ferroelectric polarization in epitaxial $BaTiO_3$ films on silicon without a conducting bottom electrode. *Nat. Nanotechnol*. **8**, 748–754 (2013).
11. Schlom, D. G. & Haeni, J. H. A thermodynamic approach to selecting alternative gate dielectrics. *MRS Bull*. **27**, 198–204 (2002).
12. Böscke, T. S., Müller, J., Bräuhaus, D., Schröder, U. & Böttger, U. Ferroelectricity in hafnium oxide thin films. *Appl. Phys. Lett*. **99**, 102903 (2011).
13. Park, M. H. et al. Ferroelectricity and antiferroelectricity of doped thin HfO_2-based films. *Adv. Mater*. **27**, 1811–1831 (2015).
14. Robertson, J. High dielectric constant gate oxides for metal oxide Si transistors. *Rep. Prog. Phys*. **69**, 327 (2006).
15. Muller, J. et al. Ferroelectric hafnium oxide: a CMOS-compatible and highly scalable approach to future ferroelectric memories. In *2013 IEEE Int. Electron Devices Meet. (IEDM)* 10.8.1–10.8.4 (IEEE, 2013).
16. Park, M., Lee, Y., Mikolajick, T., Schroeder, U. & Hwang, C. Review and perspective on ferroelectric HfO_2-based thin films for memory applications. *MRS Commun*. **8**, 795–808 (2018).
17. Wong, J. C. & Salahuddin, S. Negative capacitance transistors. *Proc. IEEE* **107**, 49–62 (2019).
18. Kwon, D. et al. Improved subthreshold swing and short channel effect in FDSOI n-channel negative capacitance field effect transistors. *IEEE Electron Device Lett*. **39**, 300–303 (2018).
19. Salahuddin, S., Ni, K. & Datta, S. The era of hyper-scaling in electronics. *Nat. Electron*. **1**, 442–450 (2018).
20. Merz, W. J. The effect of hydrostatic pressure on the Curie point of barium titanate single crystals. *Phys. Rev*. **78**, 52 (1950).
21. Ohtaka, O. et al. Phase relations and volume changes of hafnia under high pressure and high temperature. *J. Am. Ceram. Soc*. **84**, 1369–1373 (2001).
22. Materlik, R., Künneth, C. & Kersch, A. The origin of ferroelectricity in $Hf_{1-x}Zr_xO_2$: a computational investigation and a surface energy model. *J. Appl. Phys*. **117**, 134109 (2015).
23. Xiao, J. et al. Intrinsic two-dimensional ferroelectricity with dipole locking. *Phys. Rev. Lett*. **120**, 227601 (2018).
24. Vasudevan, R. K., Balke, N., Maksymovych, P., Jesse, S. & Kalinin, S. V. Ferroelectric or non-ferroelectric: why so many materials exhibit "ferroelectricity" on the nanoscale. *Appl. Phys. Rev*. **4**, 021302 (2017).
25. Balke, N. et al. Differentiating ferroelectric and nonferroelectric electromechanical effects with scanning probe microscopy. *ACS Nano* **9**, 6484–6492 (2015).
26. Collins, L., Liu, Y., Ovchinnikova, O. S. & Proksch, R. Quantitative electromechanical atomic force microscopy. *ACS Nano* **13**, 8055–8066 (2019).
27. Disa, A. S. et al. Orbital engineering in symmetry-breaking polar heterostructures. *Phys. Rev. Lett*. **114**, 026801 (2015).
28. Wei, Y. et al. A rhombohedral ferroelectric phase in epitaxially strained $Hf_{0.5}Zr_{0.5}O_2$ thin films. *Nat. Mater*. **17**, 1095–1100 (2018).
29. Lyu, J., Fina, I., Solanas, R., Fontcuberta, J. & Sánchez, F. Growth window of ferroelectric epitaxial $Hf_{0.5}Zr_{0.5}O_2$ thin films. *ACS Appl. Electron. Mater*. **1**, 220–228 (2019).
30. Schlom, D. G. et al. Elastic strain engineering of ferroic oxides. *MRS Bull*. **39**, 118–130 (2014).
31. Park, M. H. et al. Evolution of phases and ferroelectric properties of thin $Hf_{0.5}Zr_{0.5}O_2$ films according to the thickness and annealing temperature. *Appl. Phys. Lett*. **102**, 242905 (2013).
32. Tian, X. et al. Evolution of ferroelectric HfO_2 in ultrathin region down to 3 nm. *Appl. Phys. Lett*. **112**, 102902 (2018).
33. Richter, C. et al. Si doped hafnium oxide—a "fragile" ferroelectric system. *Adv. Electron. Mater*. **3**, 1700131 (2017).
34. Stengel, M. & Spaldin, N. A. Origin of the dielectric dead layer in nanoscale capacitors. *Nature* **443**, 679–682 (2006).
35. Kim, S. J., Mohan, J., Summerfelt, S. R. & Kim, J. Ferroelectric $Hf_{0.5}Zr_{0.5}O_2$ thin films: a review of recent advances. *JOM* **71**, 246–255 (2019).
36. Schlom, D. G. et al. Strain tuning of ferroelectric thin films. *Annu. Rev. Mater. Res*. **37**, 589–626 (2007).
37. Haeni, J. H. et al. Room-temperature ferroelectricity in strained $SrTiO_3$. *Nature* **430**, 758–761 (2004).
38. Zubko, P., Catalan, G. & Tagantsev, A. K. Flexoelectric effect in solids. *Annu. Rev. Mater. Res*. **43**, 387–421 (2013).
39. Jariwala, D., Marks, T. J. & Hersam, M. C. Mixed-dimensional van der Waals heterostructures. *Nat. Mater*. **16**, 170–181 (2017).
40. Kwon, D. et al. Negative capacitance FET with 1.8-nm-thick Zr-doped HfO_2 oxide. *IEEE Electron Device Lett*. **40**, 993–996 (2019).
41. Lee, M. H. et al. Physical thickness 1.x nm ferroelectric $HfZrO_x$ negative capacitance FETs. In *2016 IEEE Int. Electron Devices Meet. (IEDM)* 12.1.1–12.1.4, https://ieeexplore.ieee.org/document/7838400/ (IEEE, 2016).

Methods

Sample deposition and preparation

Thin films of $Hf_{0.8}Zr_{0.2}O_2$ were grown by ALD in a Fiji Ultratech/Cambridge Nanotech tool at 250 °C, in which tetrakis (ethylmethylamino) hafnium and tetrakis (ethylmethylamino) zirconium precursors are heated to 75 °C and water vapour is used as the oxidant. For metal-ferroelectric-insulator-semiconductor structures, heavily p-doped Si(100) substrates (10^{19} cm^{-3}) are first oxidized in ambient O_2 during an rapid thermal annealing step at 900 °C for 60 s, forming about 2 nm of thermal SiO_2 on Si. For metal-ferroelectric-metal structures, the Si substrate is coated with 30 nm TiN. Subsequently, HZO is deposited at 250 °C by ALD; a 4:1 ratio between the HfO_2 monolayer and the ZrO_2 monolayer sets the 80:20 stoichiometry of the deposited HZO, in which ten cycles corresponds to 1 nm of film. After ALD deposition, a top metal (W or TiN) is deposited by sputtering at room temperature. Finally, a rapid post-metal annealing at 500 °C (30 s, ambient N_2 background) stabilizes the desired polar orthorhombic phase. For capacitor structures (scanning probe studies), the top electrodes are defined by photolithography and dry etching. For bare structures (structural studies), the top metal is removed by chemical etching to expose the HZO surface. Further details pertaining to ALD growth conditions, post-deposition processing, and so on are outlined in a previous work[42]. All thin film synthesis was performed at University of California, Berkeley; processing was performed at the Marvell Nanofabrication Laboratory at University of California, Berkeley. One nanometre of chemically grown SiO_2 on Si was prepared by the standard clean (SC-1) solution (5:1:1 H_2O:H_2O_2:NH_4OH at 80 °C for 10 min) after the Si wafer was cleaned in Piranha (120 °C for 10 min) to remove organics and HF (50:1 H_2O:HF at room temperature for 30 s) to remove any native oxide. Thinner SiO_2 was employed to help reduce depolarization fields and improve the electric field distribution through the ultrathin ferroelectric HZO layer.

Electron microscopy

Electron microscopy was performed at the National Center for Electron Microscopy facility of the Molecular Foundry at LBNL as well as by Nanolab Technologies Inc., a commercial vendor. At the National Center for Electron Microscopy, TEM samples were prepared by mechanical polishing on an Allied High Tech Multiprep and subsequently Ar ion milled using a Gatan Precision Ion Milling System at shallow angles (5° to 3°) with starting energies of 5 keV stepped down to a final cleaning energy of 200 eV to reduce ion-induced damage. High-angle annular dark-field (HAADF) scanning transmission electron microscopy (STEM) images were recorded on TEAM I, an aberration-corrected FEI Titan 80–300 operated in STEM mode at 300 kV with a convergence semi-angle of 17 mrad, 70 pA probe current, and collection angles >40 mrad. The local thicknesses of the respective HZO layers were determined from calibration to the Si(110) interplanar lattice spacing (Extended Data Fig. 3), consistent with global thicknesses extracted using XRR (Extended Data Fig. 2).

Scanning probe microscopy

Piezoresponse microscopy and spectroscopy. PFM measurements (Extended Data Figs. 6, 7) were performed using a commercial scanning probe microscope (Asylum MFP-3D) at the University of California, Berkeley. Dual-frequency resonance-tracking PFM[43] was conducted using a conductive Pt/Ir-coated probe tip (NanoSensor PPP-EFM) to image written domain structures and measure switching-spectroscopy[44] piezoelectric hysteresis loops. Resonance-enhanced PFM increases the signal-to-noise ratio for the detection of out-of-plane electric polarization, which is critical for ultrathin films. Contact was made to the bottom TiN electrode or heavily doped Si substrate for grounding in PFM studies. All PFM phase-contrast images and hysteresis loops shown were performed on ten-cycle (about 1 nm) HZO films unless otherwise indicated. PFM imaging was performed with the tip in direct contact with the HZO layer. Switching-spectroscopy hysteresis loops were measured on capacitor structures to help eliminate electrostatic artefacts from the tip[45], mitigate possible electromechanical contributions[24], and to yield more confined electric fields. V_{ac}-dependent piezoresponse loops (Extended Data Fig. 7c) examined the ferroelectric origin of the PFM signal—as opposed to tip bias-induced artefacts[25]—in ultrathin HZO films. The piezoresponse OFF loop collapsed once V_{ac} exceeded the coercive voltage[46], as expected for ferroelectric behaviour. Piezoresponse is defined as $A\cos\theta$, where A and θ are the PFM amplitude and phase, respectively[45]. We note that the non-ideal shape of the piezoresponse loops, particularly at higher voltages, are caused by non-ferroelectric artefacts from the additional dielectric SiO_2 layer through which most of the voltage is dropped. For all PFM studies, the bias was applied to the tip.

Effective coercive field. The switching voltage from PFM loops exaggerate the coercive field of the ultrathin HZO layer once considering the potential distribution across the modified metal-oxide-semiconductor structure (oxide bilayer SiO_2-HZO). The effective coercive field of the HZO layer can be determined using a simple dielectric-ferroelectric bilayer model, ignoring accumulation and depletion regions at the moment just to approximate the coercive field. Considering appropriate electrical boundary conditions across the oxide interface ($\epsilon_{DE}E_{DE} = \epsilon_{FE}E_{FE}$), the voltage across the ferroelectric layer (V_{FE}) can be expressed in terms of the total voltage given by the PFM loop (V_{tot}):

$$V_{FE} = \left(1 + \frac{t_{DE}}{t_{FE}}\frac{\epsilon_{FE}}{\epsilon_{DE}}\right)^{-1} V_{tot}$$

where the dielectric constant for the oxide layers are taken as $\epsilon_{DE} = 3.9$ (SiO_2) and as $\epsilon_{FE} = 24$ (HZO)[4,14] and the thicknesses of the oxide layers are $t_{DE} = 2$ nm and $t_{FE} = 1$ nm. These values yield $V_{FE} = V_{tot}/13$, so the effective coercive field of the ten-cycle (1 nm) ferroelectric HZO layer is approximately 2 MV cm^{-1}, consistent with values of thicker HZO films reported in the literature[13].

Interferometry. IDS PFM measurements (Extended Data Fig. 7d) were performed using a commercial scanning probe microscope (Asylum Cypher) with an integrated quantitative laser Doppler vibrometer at Asylum Research (Santa Barbara). This recently developed method[26] eliminates crosstalk and other artefacts present in voltage-modulated piezo-measurements (d_{33}) by replacing the typical slope-sensitive optical beam detector with a displacement sensitive interferometer. By positioning the IDS laser directly over the tip, motion of the tip can be decoupled from spurious motion of the cantilever body. Motion of the cantilever body can be driven by long-range electrostatics and is influenced by the transfer function of the cantilever[26]. IDS measurements were performed with a 3 N m^{-1} Ti/Ir coated cantilever placed on the bare 1-nm HZO surface at drive frequency 250 kHz and average force 75 nN. Off-surface loops (tip raised from surface), which measure the extrinsic electrostatic contributions[26], were performed by changing the trigger value from deflection (force) to the z-sensor read-out. The lack of hysteresis from off-surface (non-contact) loops further support the finding that the hysteresis observed from on-contact IDS measurements are free from electrostatic contributions. Typical voltage-modulated PFM measurements often display false ferroelectric hysteresis due to long-range cantilever dynamics inherent to detection by the optical beam detector, as observed from non-contact hysteresis in non-piezoelectric samples[26].

Microwave capacitance. SCM measurements (Extended Data Fig. 8c) were performed using a commercial scanning probe microscope (Asylum Cypher) at Asylum Research (Santa Barbara). Differential capacitance (dC/dV) measurements were performed at 1.8-GHz frequency with a 40 kHz lock-in frequency at 0.5 V_{ac}. Pure Pt cantilevers (Rocky Mountain Nanotechnology) are placed on top of bare HZO surface (contact mode) on TiN-buffered Si for SCM measurements; dC/dV signals were extracted via V_{ac} applied between the SCM tip and bottom electrode. Capacitance–voltage loops via SCM have been previously used to confirm ferroelectricity in $SrBi_2Ta_2O_9$ (SBT) thin films[47]. The microwave-frequency nature of the measurement lends itself to probing ultrathin ferroelectrics, as it mitigates leakage contributions. For SCM measurements, the bias was applied to the sample (swept up to ±8 V), not to the tip as is done for PFM measurements.

X-ray diffraction

Structural characterization. Synchrotron GI-XRD (Extended Data Fig. 4a) was performed at the Sector 33-BM-C beamline of the Advanced Photon Source, Argonne National Laboratory. Using synchrotron GI-XRD, we investigated the structural evolution from polycrystalline bulk-like (100-cycle) HZO down to highly textured ultrathin (<25 cycles) HZO in its polar orthorhombic ($Pca2_1$) phase, at grazing angle $\leq\theta = 0.35°$. The high flux from the synchrotron source ($\lambda = 0.775$ Å) enabled collection of sufficient diffraction intensity from the few crystallographic planes present in ultrathin HZO samples. High-resolution GI-XRD was also performed using a laboratory-based Panalytical X'Pert Pro X-ray diffraction system (Cu K_α radiation, $\lambda = 1.54056$ Å) on HZO films thicker than 2 nm at grazing angle $\theta = 0.35°$. Previous work employed selected area electron diffraction[48] and convergent beam electron diffraction[49] to attribute ferroelectricity in HfO_2-based films to the polar orthorhombic ($Pca2_1$) phase. The indexing of ultrathin HZO films performed in this work is consistent with the same polar orthorhombic phase determined from these previous electron diffraction studies.

Texture analysis. Pole figures (Extended Data Fig. 4b) were measured at Sector 33-BM-C beamline of the Advanced Photon Source, Argonne National Laboratory. For fixed Q values—corresponding to the d_{111} lattice spacing—the 4-circle Huber diffractometer rotated in-plane (φ) 360° at multiple values of out-of-plane tilt (χ). The PILATUS 100K pixel area detector collected volumetric reciprocal space data from which two-dimensional pole figure slices were plotted for shells of constant Q_z. The four concentrated reflections for the {111} projection in Q_x–Q_y space indicate highly oriented texture, rather than the diffuse rings expected for polycrystalline films. As indicated in the main text (Fig. 3), films thinner than 25 cycles display substantial texturing (Extended Data Fig. 4); in particular, the (111) reflection, which is dominant for thicker films, is diminished in GI-XRD spectra of ultrathin films owing to the geometric limitations of a one-dimensional pattern (it is unable to detect all reflections present in oriented films). This limitation necessitates tilted-geometry two-dimensional patterns (pole figures) in order to detect all reflections present in highly oriented films. Meanwhile, reflections corresponding to polycrystalline films exhibit continuous rings in two-dimensional Q_x–Q_y reciprocal space, so any one-dimensional line-cut (GI-XRD spectra) would detect all reflections present. The results on ultrathin HZO films are in stark contrast to results on thicker films[50,51] and indicate that, for such ultrathin films, crystallization and orientation need to be considered together. We also observed that for such thin films, the template for HZO growth needs to be atomically smooth. Therefore, the Si/SiO_2 interface employed in this work is critical; the growth surface is expected to have a larger role for ultrathin films than for thicker films.

Thickness confirmation. Synchrotron XRR of ultrathin HZO films (Extended Data Fig. 2)—performed at Sector 33-BM-C beamline of the Advanced Photon Source, Argonne National Laboratory and at Beamline 2-1 of the Stanford Synchrotron Radiation Lightsource, SLAC National Accelerator Laboratory—confirmed the thickness of sub-2-nm films. Fitting analysis was performed with the Python package xrayutilities[52]. XRR of thicker HZO films (>2 nm) was measured with the Panalytical X'Pert Pro system, and thickness fitting was performed with Panalytical software. The extracted growth rate of 11 cycles nm^{-1} is consistent with results from TEM and literature[13].

Structural distortion analysis. For the polar orthorhombic phase ($Pca2_1$), we consider the orthorhombic distortion (that is, orthorhombicity) as the aspect ratio: $2c/(a+b)$ to enable easier comparison to the tetragonal ($P4_2/nm$) aspect ratio c/a. Fluorite-structure orthorhombicity is meant to be analogous to the perovskite ferroelectric tetragonality (c/a, where c is the polar axis); both aspect ratios serve as a structural gauge of the macroscopic polarization because they are indicative of the polar distortion present in their respective structures[53]. Notably, the orthorhombic distortion present in HZO is enhanced in the ultrathin regime—opposite to the typical tetragonal distortion trend in perovskite ferroelectrics[6]—indicative of the 'reverse' size effects present in fluorite-structure ferroelectrics. For example, the tetragonal aspect ratio was shown to decrease with decreasing thickness in ferroelectric $PbTiO_3$ films[53], while the orthorhombic aspect ratio is greatly enhanced in the ultrathin regime in our fluorite-structure HZO films (Fig. 3g). The orthorhombic distortion present in ten-cycle (about 1 nm) HZO far exceeds any reported values for HfO_2-ZrO_2 polymorphs: we find >11% aspect asymmetry, while 3–4% is typically reported for fluorite-structure ferroelectrics[31], consistent with our thicker films (Fig. 3g). Indeed, a strong relationship between this aspect ratio and the remanent polarization value has been experimentally demonstrated in thicker doped HfO_2 films[54]. Therefore, the colossal orthorhombic aspect ratio present in ten-cycle HZO is consistent with ultrathin-enhanced ferroelectricity. The orthorhombic aspect ratio is calculated from the position of various diffraction peaks indexed to the $Pca2_1$ phase (the 200, 020 and 002 peaks), using the following crystallographic relations: $a = 2\cdot d_{200}$, $b = 2\cdot d_{020}$, $c = 2\cdot d_{002}$ where d_{200}, d_{020}, and d_{002} are the 200, 020 and 002 lattice spacings determined via Bragg's law and the respective peak positions. These values are self-consistently checked against the 111 interplanar lattice spacing ($1/d_{111}^2 = 1/a^2 + 1/b^2 + 1/c^2$) as well as against other orientations present in the diffraction spectra. The aspect ratio of the polar O-phase exceeds that of the T-phase (c/a) for doped HfO_2[54]. Another structural marker indicates amplified distortions as thickness is reduced, namely the interplanar lattice spacing d_{111}. The origin of the left shift in the O-phase 111 (T-phase 101) reflection (Fig. 3f) with decreasing thickness (that is, decreasing ALD cycles) is typically attributed to the abovementioned phase transition (nonpolar T-phase to polar O-phase); the left shift of the peak in reciprocal space corresponds to an increase in real-space lattice spacing. Extending this analogy to the ultrathin regime in which the polar O-phase is already stabilized, the ultrathin enhancement of d_{111} (Fig. 3g) indicates a further increase in rhombic distortion (structurally represented by d_{111}). Recent works on epitaxial HZO films grown by high-temperature pulsed laser deposition on perovskite substrates also indicate increasing d_{111} with decreasing thickness[28,29]; these works find the electric polarization to increase with increasing d_{111}. Similarly, we expect a larger polarization in our ultrathin films based on the d_{111} trend (Fig. 3g); notably, our low-temperature ALD-grown highly oriented films are mimicking the trends observed in high-temperature pulsed-laser-deposition-grown epitaxial films.

X-ray spectroscopy

XAS and XLD. X-ray absorption spectroscopy (XAS) and XLD was performed at the Advanced Light Source beamline 4.0.2. XAS measurements were taken at the oxygen K edge (520–550 eV) and Zr M_2 edge (345–355 eV). X-rays were incident at 20° off grazing. XLD (XAS) was obtained from the difference (average) of horizontal and vertical linearly polarized X-rays. To eliminate systematic artefacts in the signal that drift with time, spectra were captured with the order of polarization rotation reversed (such as horizontal, vertical, vertical and horizontal) in successive scans. An elliptically polarizing undulator was used to tune polarization and photon energy of the synchrotron X-ray source[55]. XAS was recorded under total electron yield mode[55].

Simulated XAS and crystal field symmetry. Simulated XAS spectra for the various fluorite-structure polymorphs were computed through the Materials Project[56] open-source database for the XAS spectrum[57]. In particular, the following symmetries for HfO_2 and ZrO_2 were investigated: monoclinic $P2_1/c$ (space group 14), orthorhombic $Pca2_1$ (space group 29), and tetragonal $P4_2/nmc$ (space group 137). Comparisons between HZO and the undoped fluorite-structure endmembers (in particular, qualitative comparison of splitting-induced spectroscopy features) are reasonable owing to the extremely low structural dissimilarity between the same polymorphs of HfO_2 and ZrO_2, as determined by pymatgen[58]. The T-phase ($P4_2/nmc$) nonpolar distortion (D_{4h}, fourfold prismatic symmetry) from regular tetrahedral (T_d, full tetrahedral symmetry) fluorite-structure symmetry does not split the degenerate *e* bands ($d_{x^2-y^2}$, $d_{3z^2-r^2}$), as confirmed by experiment[59] and the XAS simulations (Extended Data Fig. 9b). Meanwhile, the O-phase ($Pca2_1$) polar rhombic pyramidal distortion (C_{2v}, twofold pyramidal symmetry) does split the *e*-manifold based on crystal field symmetry (Extended Data Fig. 9b), providing a spectroscopic means to distinguish the T- and O-phases. The eightfold Hf-O (Zr-O) coordination (Extended Data Fig. 9d) in the tetragonal phase (D_{2d} point group symmetry) can be decomposed into two tetrahedra that are the space inversion twins of one another. Therefore, crystal field splitting of the *e* levels matches that of a single tetrahedron[59]—that is, there is no further splitting. Meanwhile, the sevenfold Hf-O (Zr-O) coordination (Extended Data Fig. 9d) in the orthorhombic phase cannot be decomposed into two tetrahedra; the additional rhombic distortion (not present in the T-phase) splits the *e* manifold. The simulated XAS spectra for T- and O-phase ZrO_2 (Extended Data Fig. 9b) supports this picture, because the additional spectroscopic feature present between the main *e*- and t_2- absorption features in the O-phase is presumably caused by this additional symmetry-lowering distortion. The XAS spectra of the HZO thickness series (Extended Data Fig. 9c) demonstrates tetrahedral and rhombic splitting features closely matching the polar O-phase ($Pca2_1$). This demonstrates a spectroscopic method for phase identification beyond diffraction—ambiguous owing to the nearly identical T- and O-phase lattice parameters[13]—whose signatures are more sensitive to the subtle structural distortions present as symmetry is lowered from the T- to the O-phase.

Crystal field splitting. Notably, the crystal field distortions present in confined HZO films greatly exceed what is typically observed in bulk fluorite-structures and perovskite ferroelectrics (Extended Data Fig. 9g); the tetrahedral (rhombic) crystal field Δ_T (Δ_R) arising from the T_d (C_{2v}) symmetry in ten-cycle HZO films is 1.3 eV (0.7 eV) greater than what is expected from fluorite-structure ZrO_2 in the polar orthorhombic phase ($Pca2_1$). The computational XAS for the $Pca2_1$ phase already takes the polar distortion (Δ_R) into account; so the enhanced Δ_R in ultrathin confined films again points to enhanced polar distortions (consistent with diffraction-based results). Kindred efforts to uncover routes towards enhanced nanoscale distortions have been explored in complex perovskite heterostructures. For example, in nickelate perovskite superlattices, enormous Δ_{eg} crystal field splitting (up to 0.8 eV) has been achieved via polar fields resulting from internal charge transfer[27]; >10% epitaxial strain would be required to induced such large ionic distortions in that particular system, well beyond the limits of epitaxial strain, which can only achieve e_g splitting of about 300 meV (ref. [60]).

Spectral weight trends. The relative spectral weight of the *e* and t_2 manifolds (Extended Data Fig. 9c) at the O *K* edge can also provide insight into the degree of structural distortion[61]. Owing to the d^0 electronic configuration present in Hf^{4+} (Zr^{4+}), all *d* states are available for mixing with O 2*p* states, so the analysis of *e*-t_2 spectral weight can be simplified to be purely due to crystal field effects[61]. Tetrahedral symmetry lowers *e* bands relative to t_2 bands due to the enhanced t_2 orbital overlap with oxygen 2*p* orbitals. The enhanced t_2/e spectral weight as thickness is reduced (Extended Data Fig. 9c) indicates the preference for O 2*p* hybridization with Hf 5*d* (Zr 4*d*) t_2 orbitals, further exaggerating the disparity set by the tetrahedral symmetry as the symmetry is lowered to the polar O-phase. Additionally, the increase in spectral weight of the pre-edge shoulder (Extended Data Fig. 9e) provides further confirmation that structural distortions are amplified in the ultrathin limit. Pre-edge features at the O *K* edge in complex transition metal oxides are commonly attributed to nearest-neighbour variations from typical oxygen polyhedral coordination as the symmetry is lowered by various distortions[62]. Analogously, here the pre-edge feature is attributed to variation from eightfold coordination in the T-phase (NN = 8) as the symmetry is lowered into the polar O-phase (NN = 7) (Extended Data Fig. 9d). On the unit cell level in the polar O-phase, the central metal cation is surrounded by an asymmetric oxygen coordination environment (note the 4 blue and 3 cyan oxygen atoms in Extended Data Fig. 9d) owing to the polar rhombic distortion of normal tetrahedral (T_d) symmetry; this polyhedral distortion can manifest as increased spectral weight at the oxygen *K* pre-edge[62]. The critical *e* manifold splitting due to the polar rhombic distortion also increases in spectral weight as thickness is reduced (Extended Data Fig. 9c). The XAS spectral weight trends mirror the structural indicators of ultrathin-enhanced distortion (Fig. 3c).

Orbital polarization. In conjunction with XAS, XLD can also probe structural distortions owing to its sensitivity to orbital asymmetry, which can arise from inversion symmetry breaking. For example, in the perovskite ferroelectrics $PbTiO_3$ and $BaTiO_3$, the Ti 3*d* to O 2*p* orbital hybridization is essential for stabilizing the noncentrosymmetric structure[63]. Particularly at the 3*d* cation $L_{3,2}$ edge, orbital polarization extracted from XLD is used as a measure of the oxygen octahedral distortion in perovskites owing to the anisotropic hybridization between cation 3*d* and O 2*p* orbitals[64]. Accordingly, in fluorite-structure ferroelectrics, the magnitude of XLD present at the Zr $M_{3,2}$ edges can be a gauge of the degree of polyhedral distortion (in this case, a distortion of the oxygen tetrahedron) and the oxygen atomic asymmetry. Indeed, the orbital polarization at the Zr M_2 edge is enhanced as the thickness is reduced from the thick (100-cycle) to ultrathin (ten-cycle) regime (Fig. 3c), consistent with diffraction-based results demonstrating amplified structural distortions in the ultrathin limit. Spectroscopy can also help understand the evolution to highly textured films in the ultrathin limit (Fig. 3e, f), as XLD enables both element- and orbital-specific information by comparing polarization-dependent XAS spectra. GI-XRD across the thickness series (Fig. 3f) indicates that the degree of orientation substantially changes as the HZO drops below about 2.5 nm (25 cycles). The microstructure change below 25 cycles also manifests as inverted orbital polarization at the oxygen *K* edge, particularly at the *e* manifold (Fig. 3b). Absorption of vertically and horizontally polarized light preferentially probes the polar-distortion-split *e* levels (the x^2y^2 and $3z^2r^2$ *d* orbitals); the reversal of XLD sign indicates these levels are inverted with respect to one another. In perovskites, such a change in orbital polarization is often attributed to different signs of tetragonal distortion (*c*/*a*) of the oxygen octahedron[64]. Analogously, here the change in microstructure across 20–25 cycles, namely, the emergence of highly oriented films, could allow confinement strain effects to distort the oxygen tetrahedron more coherently along the polar axis. This synergistic effect could potentially explain the enhanced distortions observed in the ultrathin regime.

Nanospectroscopy. PEEM was performed at the Advanced Light Source beamline 11.0.1. X-rays were incident at 30° off grazing, probing just the first few nanometres of film, spanning the entire ten-cycle (1 nm) HZO thickness. Nanospectroscopy point-by-point scans were employed to spatially resolve XLD contrast; at each specified energy value in the oxygen *K* edge (520–550 eV) regime, PEEM images were taken for both values of the linear polarization (horizontal, vertical) across a 20-μm field of view (1,000 × 1,000 pixel grid). The exposure to high-flux synchrotron X-rays probably depolarized the ultrathin ferroelectric sample as photoelectrons were removed from the surface, as is observed in ultrathin films of $BaTiO_3$ and other ferroelectrics; PEEM-XLD images (Extended Data Fig. 9f) illustrate nanoscale domains at the energy range corresponding to the polar *e*-split feature. Data processing to extract XLD contrast involved dividing images of opposite linear polarization, which eliminates topography and work function contrast. Topography and work function artefacts contribute at the pre-edge (about 530 eV), whereas the intrinsic orbital anisotropy contributions manifest only at resonance (about 535 eV); the presence of XLD contrast only at resonance confirms the orbital asymmetry origins of XLD contrast in ultrathin HZO. Furthermore, the highly textured nature of the ultrathin films prevents the XLD contrast from averaging to zero (cancellation would be expected for a fully polycrystalline film) on a length scale smaller than the experimental resolution.

Optical spectroscopy

SHG and inversion asymmetry. Nonlinear optical SHG was performed using a custom setup at University of California, Berkeley, as detailed in a previous work[23]. The excitation light was extracted using an optical parametric oscillator (Inspire HF 100, Spectra Physics, Santa Clara) pumped by a mode-locked Ti:sapphire oscillator. The excitation laser was linearly polarized by a 900–1,300 nm polarizing beamsplitter. The transmitted *p*-polarized laser light can change its polarization by rotating an infrared half waveplate before pumping the sample. The laser is focused by a 50× near-infrared objective onto the sample. The SHG signal was detected in the backscattering configuration, analysed by a visible-range polarizer, and finally collected by a cooled charge-coupled device spectrometer. SHG was performed with a 960-nm pump and detected at 480 nm under tilt incidence. SHG is commonly used to investigate piezoelectric and ferroelectric single crystals and thin films[65] as the photon frequency-doubling process is allowed only in materials lacking inversion symmetry.

Field-dependent SHG. Electric-field-dependent SHG experiments were performed on the bare surface of ten-cycle (1 nm) HZO films (top metal was etched away after phase annealing). The HZO layer was then patterned into micrometre-sized islands to enable systematic identification of specific HZO regions; various islands were poled with an electric field (applied by a PFM tip), while other islands were left as is. The optical microscope identified the poled and unpoled islands, and the second harmonic signal was detected across various islands. Increased SHG intensity, sensitive to out-of-plane polarization in this tilt-incidence experimental geometry, in poled HZO islands suggests that the electric field increases the projection of out-of-plane polarization by aligning domains with different polarization directions.

Electrical characterization

Tunnel current measurements. Tunnel current measurements were performed using a commercial Semiconductor Device Analyzer (Agilent B1500) with a pulse generator unit to enable voltage pulses down to the microsecond regime. Samples were patterned into capacitors of various area, with W as the top electrode, and heavily doped Si (10^{19} cm^{-3}) as the bottom contact. The 19-μm W tips (DCP-HTR 154-001, FormFactor) made electrical contact within a commercial probe station (Cascade Microtech). In tandem, conducting atomic force microscopy measurements were performed using a commercial scanning probe microscope (Asylum MFP-3D) at University of California, Berkeley. Current–voltage characteristics through the capacitor device were probed in the AFM by using a Keithley 2400 Source Measure Unit to bias the top electrode of the sample through 20-nm-radii Pt/Ir-coated AFM probes (25PtIr300B cantilever probe, Rocky Mountain Nanotechnology), grounded to the heavily doped Si substrate.

Current–voltage hysteresis and tunnel electroresistance. We used voltage-polarity-dependent current–voltage hysteresis to rule out resistive switching mediated by dielectric breakdown and filamentary-type switching. For filamentary-mediated resistive switching—often observed in amorphous HfO_2—the sense of hysteresis is dependent on the direction of the voltage sweep (that is, the initial polarity of the voltage waveform), which dictates the filament formation[66]. Meanwhile, ferroelectric tunnel junctions demonstrate the same sense of current–voltage hysteresis independent of the sweep direction; this voltage-polarity independence is indicative of polarization-mediated switching, as observed for our ultrathin ten-cycle (1 nm) HZO films (Extended Data Fig. 10e). To further investigate the origin of the resistive switching, tunnelling electroresistance hysteresis maps as a function of write voltage (at low read voltage) demonstrate saturating, abrupt hysteretic behaviour (Extended Data Fig. 10b, d) characteristic of polarization-driven switching[67,68]. Evidence of polarization-driven resistive switching from tunnelling electroresistance is provided for ten-cycle (1 nm) HZO films of two different compositions (Extended Data Fig. 10). Although many of the results presented here are for films with 4:1 Hf:Zr ratio, for comparison, we have included results and demonstrated ferroelectricity for a ten-cycle (1 nm) film with this modified 1:1 Hf:Zr ratio. Pioneering work on HZO in the thicker regime (>5 nm)[50,69,70] has shown that a 1:1 Hf:Zr ratio often demonstrates the best ferroelectric properties. Ferroelectric tunnel junctions based on composite ferroelectric-dielectric barriers using HZO in this thicker regime demonstrate promising polarization-driven resistive switching results[71,72]. Optimizing ferroelectric tunnel junction behaviour employing HZO in the ultrathin regime (around 1 nm) will need to be carefully studied.

Data availability

The datasets generated during and/or analysed during the current study are available from the corresponding author on reasonable request.

42. Karbasian, G. et al. Stabilization of ferroelectric phase in tungsten capped $Hf_{0.8}Zr_{0.2}O_2$. *Appl. Phys. Lett.* **111**, 022907 (2017).
43. Rodriguez, B. J., Callahan, C., Kalinin, S. V. & Proksch, R. Dual-frequency resonance-tracking atomic force microscopy. *Nanotechnology* **18**, 475504 (2007).
44. Jesse, S., Lee, H. N. & Kalinin, S. V. Quantitative mapping of switching behavior in piezoresponse force microscopy. *Rev. Sci. Instrum.* **77**, 073702 (2006).
45. Hong, S. et al. Principle of ferroelectric domain imaging using atomic force microscope. *J. Appl. Phys.* **89**, 1377–1386 (2001).
46. Strelcov, E. et al. Role of measurement voltage on hysteresis loop shape in piezoresponse force microscopy. *Appl. Phys. Lett.* **101**, 192902 (2012).
47. Leu, C.-C. et al. Domain structure study of $SrBi_2Ta_2O_9$ ferroelectric thin films by scanning capacitance microscopy. *Appl. Phys. Lett.* **82**, 3493–3495 (2003).
48. Chernikova, A. et al. Ultrathin $Hf_{0.5}Zr_{0.5}O_2$ ferroelectric films on Si. *ACS Appl. Mater. Interf.* **8**, 7232–7237 (2016).
49. Sang, X., Grimley, E. D., Schenk, T., Schroeder, U. & LeBeau, J. M. On the structural origins of ferroelectricity in HfO_2 thin films. *Appl. Phys. Lett.* **106**, 162905 (2015).
50. Böscke, T. *Crystalline Hafnia and Zirconia Based Dielectrics for Memory Applications* PhD thesis, Hamburg University of Technology, https://cuvillier.de/en/shop/publications/763-crystalline-hafnia-and-zirconia-based-dielectrics-for-memory-applications (2010).
51. Zhao, C., Roebben, G., Heyns, M. M. & Van der Biest, O. Crystallisation and tetragonal-monoclinic transformation in ZrO_2 and HfO_2 dielectric thin films. *Key Eng. Mater.* **206–213**, 1285–1288 (2001).
52. Kriegner, D., Wintersberger, E. & Stangl, J. xrayutilities: a versatile tool for reciprocal space conversion of scattering data recorded with linear and area detectors. *J. Appl. Cryst.* **46**, 1162–1170 (2013).
53. Lichtensteiger, C., Triscone, J., Junquera, J. & Ghosez, P. Ferroelectricity and tetragonality in ultrathin $PbTiO_3$ films. *Phys. Rev. Lett.* **94**, 047603 (2005).
54. Park, M. H. et al. A comprehensive study on the structural evolution of HfO_2 thin films doped with various dopants. *J. Mater. Chem. C* **5**, 4677–4690 (2017).
55. Young, A. T. et al. Variable linear polarization from an x-ray undulator. *J. Synch. Rad.* **9**, 270–274 (2002).
56. Jain, A. et al. The Materials Project: a materials genome approach to accelerating materials innovation. *APL Mater.* **1**, 011002 (2013).
57. Mathew, K. et al. High-throughput computational X-ray absorption spectroscopy. *Sci. Data* **5**, 180151 (2018).

58. Ong, S. P. et al. Python Materials Genomics (pymatgen): a robust, open-source Python library for materials analysis. *Comput. Mater. Sci*. **68**, 314–319 (2013).
59. Cho, D.-Y., Jung, H.-S. & Hwang, C. S. Structural properties and electronic structure of HfO_2-ZrO_2 composite films. *Phys. Rev. B* **82**, 094104 (2010).
60. Wu, M. et al. Strain and composition dependence of orbital polarization in nickel oxide superlattices. *Phys. Rev. B* **88**, 125124 (2013).
61. de Groot, F. et al. Oxygen 1s X-ray-absorption edges of transition-metal oxides. *Phys. Rev. B* **40**, 5715–5723 (1989).
62. de Groot, F. Multiplet effects in X-ray spectroscopy. *Coord. Chem. Rev*. **249**, 31–63 (2005).
63. Cohen, R. E. Origin of ferroelectricity in perovskite oxides. *Nature* **358**, 136–138 (1992).
64. Pesquera, D. et al. Surface symmetry-breaking and strain effects on orbital occupancy in transition metal perovskite epitaxial films. *Nat. Commun*. **3**, 1189 (2012).
65. Denev, S. A., Lummen, T. T. A., Barnes, E., Kumar, A. & Gopalan, V. Probing ferroelectrics using optical second harmonic generation. *J. Am. Ceram. Soc*. **94**, 2699–2727 (2011).
66. Bersuker, G. & Gilmer, D. Metal oxide resistive random-access memory (RRAM) technology. In *Advances in Non-Volatile Memory and Storage Technology* 288–340 (Elsevier, 2014).
67. Chanthbouala, A. et al. Solid-state memories based on ferroelectric tunnel junctions. *Nat. Nanotechnol*. **7**, 101–104 (2012).
68. Gruverman, A. et al. Tunneling electroresistance effect in ferroelectric tunnel junctions at the nanoscale. *Nano Lett*. **9**, 3539–3543 (2009).
69. Müller, J. et al. Ferroelectricity in simple binary ZrO_2 and HfO_2. *Nano Lett*. **12**, 4318–4323 (2012).
70. Park, M. H. et al. Surface and grain boundary energy as the key enabler of ferroelectricity in nanoscale hafnia-zirconia: a comparison of model and experiment. *Nanoscale* **9**, 9973–9986 (2017).
71. Fujii, S. et al. First demonstration and performance improvement of ferroelectric HfO_2-based resistive switch with low operation current and intrinsic diode property. In *2016 IEEE Symposium on VLSI Technology* 1–2 (IEEE, 2016).
72. Max, B., Hoffmann, M., Slesazeck, S. & Mikolajick, T. Ferroelectric tunnel junctions based on ferroelectric-dielectric $Hf_{0.5}Zr_{0.5}O2/Al_2O_3$ capacitor stacks. In *2018 48th European Solid-State Device Research Conference (ESSDERC)* 142–145 (IEEE, 2018).

Acknowledgements This research was supported in part by the Berkeley Center for Negative Capacitance Transistors (BCNCT), ASCENT (Applications and Systems-Driven Center for Energy-Efficient Integrated NanoTechnologies), one of the six centres in the JUMP initative (Joint University Microelectronics Program), an SRC (Semiconductor Research Corporation) programme sponsored by DARPA, the DARPA T-MUSIC (Technologies for Mixed-mode Ultra Scaled Integrated Circuits) programme and the UC MRPI (University of California Multicampus Research Programs and Initiatives) project. This research used resources of the Advanced Photon Source, a US Department of Energy (DOE) Office of Science User Facility operated for the DOE Office of Science by Argonne National Laboratory under contract number DE-AC02-06CH11357. This research used resources of the Advanced Light Source, which is a DOE Office of Science User Facility under contract number DE-AC02-05CH11231. Use of the Stanford Synchrotron Radiation Light source, SLAC National Accelerator Laboratory, is supported by the US DOE, Office of Science, Office of Basic Energy Sciences under contract number DE-AC02-76SF00515. Electron microscopy was performed at the Molecular Foundry, LBNL, supported by the Office of Science, Office of Basic Energy Sciences, US DOE (DE-AC02-05CH11231). J.C. and R.d.R. acknowledge additional support from the Presidential Early Career Award for Scientists and Engineers (PECASE) through the US DOE. J.X and X.Z acknowledge support from the National Science Foundation (NSF) under grant 1753380 and the King Abdullah University of Science and Technology (KAUST) Office of Sponsored Research award OSR-2016-CRG5-2996.

Author contributions Film synthesis was performed by S.S.C., G.K. and D.K. Device fabrication was performed by D.K. Electron microscopy was performed by R.d.R. and S.-L.H. under the supervision of J.C. and R.R., respectively, and analysis was performed by L.-C.W. under the supervision of S.S. Scanning probe microscopy was performed by S.S.C. and N.S. IDS measurements were performed and developed by R.W. and R.P. SCM was performed by H.Z. X-ray structural characterization was performed by S.S.C., N.S. and M.R.M. under the supervision of A.M. and E.K. X-ray spectroscopy and microscopy was performed by S.S.C. under the supervision of R.V.C., P.S. and E.A. Second harmonic generation was performed by J.X. under the supervision of X.Z. Electrical measurements were performed by S.S.C., N.S. and A.D. S.S.C. and S.S. co-wrote the manuscript. S.S. supervised the research. All authors contributed to discussions and commented on the manuscript.

Competing interests The authors declare no competing interests.

Additional information

Supplementary information is available for this paper at https://doi.org/10.1038/s41586-020-2208-x.

Correspondence and requests for materials should be addressed to S.S.C. or S.S.

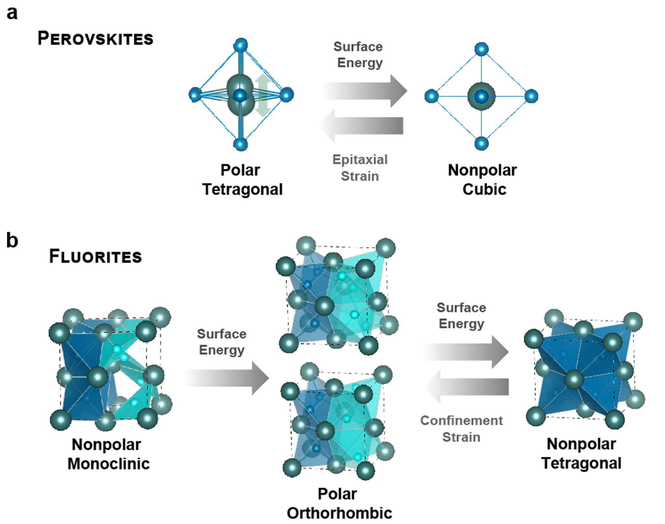

Extended Data Fig. 1 | Size effects in fluorite- and perovskite-structure ferroelectrics. a, In perovskite ferroelectrics, the polar 'tetragonal' distortion (c/a) can be represented as the centre cation displacement with respect to its surrounding oxygen octahedron. **b**, In fluorite-structure ferroelectrics, the polar 'rhombic' distortion ($2c/(a+b)$) can be represented as the centre anion displacement with respect to its surrounding cation tetrahedron; in the nonpolar T-phase, the oxygen atom (blue) lies in the polyhedral centre of the tetrahedron. The evolution of the bulk-stable M-phase to the high-symmetry T-phase and polar O-phase in the fluorite-structure structure illustrates the role of size effects (surface energies favour higher symmetry) and confinement strain (distortions favour lower symmetry) on stabilizing inversion asymmetry. Surface energies are critical when considering the role of size effects on ferroelectricity; higher-symmetry phases are energetically favourable at reduced dimensions owing to lower unit cell volumes. In fluorite structures (perovskites), the noncentrosymmetric O-phase (T-phase) has higher (lower) symmetry than the bulk-stable centrosymmetric M-phase (C-phase). Consequently, surface energies help to counteract depolarization fields in fluorite-structure ferroelectrics—already diminished in fluorite structures relative to perovskites owing to its lower dielectric constant[4]—in the ultrathin regime. Therefore, both intrinsic (surface energies) and extrinsic (confinement strain) mechanisms can favour ultrathin inversion symmetry breaking in fluorite structures. Meanwhile, both surface and depolarization energies tend to destabilize inversion asymmetry in perovskite ferroelectrics, while epitaxial strain can stabilize symmetry-lowering polar distortions[36].

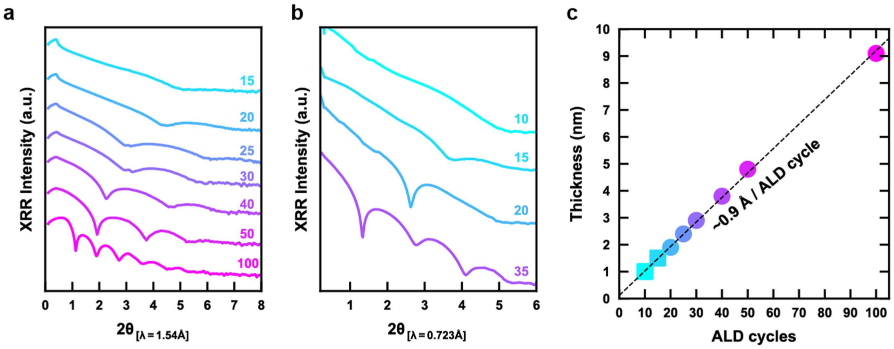

Extended Data Fig. 2 | Thickness verification of ultrathin HZO films from XRR. a, Laboratory diffractometer XRR of HZO thickness series, demonstrating clear fringes for thickness extraction present down to 20-cycle HZO. **b**, Synchrotron XRR of ultrathin HZO films, enabling thickness fitting analysis for sub-20-cycle films. **c**, HZO thickness as a function of ALD cycles, as determined by fitting analysis from XRR. The growth rate is about 11 cycles nm^{-1}, verified across 10–100 ALD cycle films. Squares (circles) represent thicknesses extracted from fitting to synchrotron (laboratory diffractometer) XRR measurements.

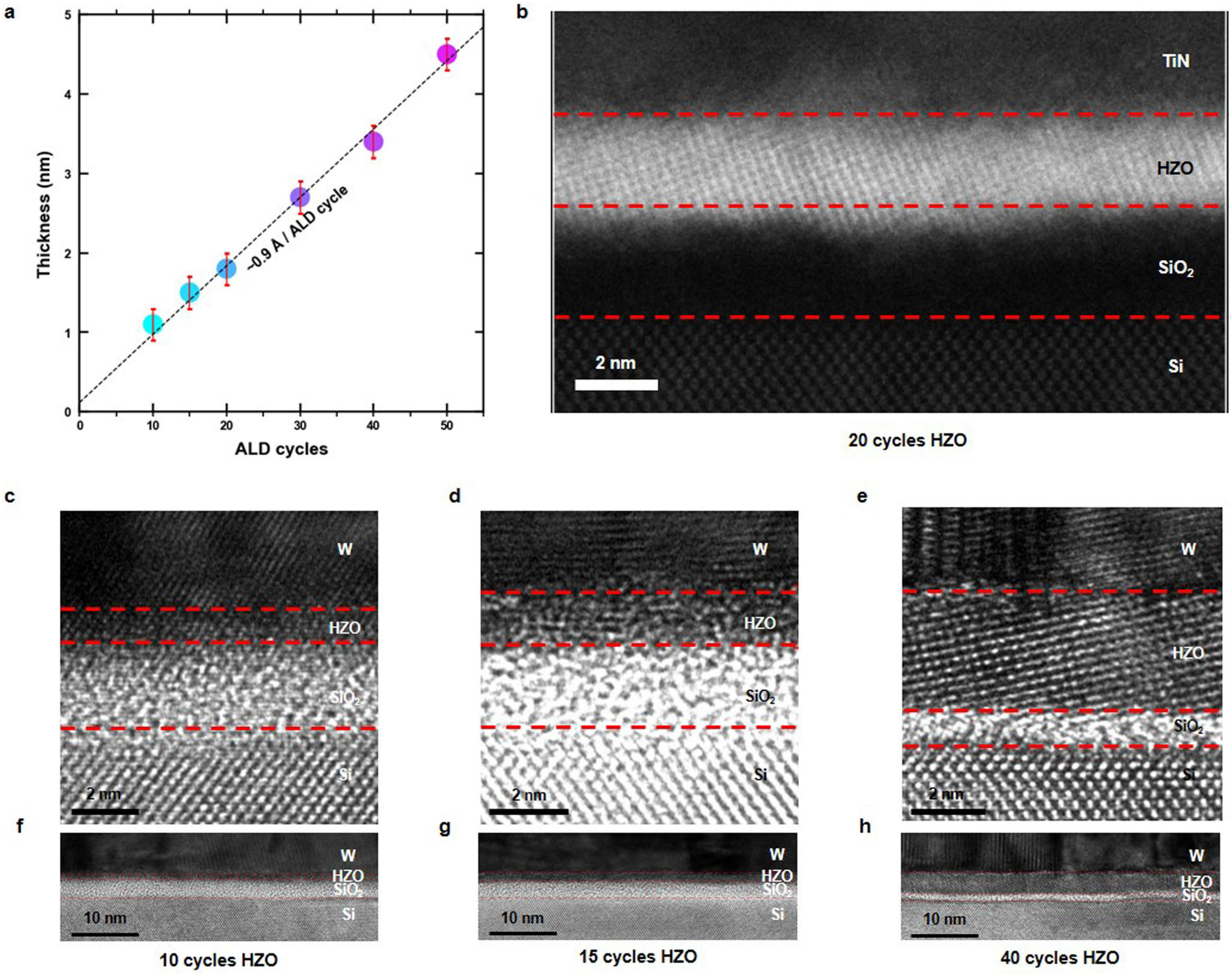

Extended Data Fig. 3 | Thickness verification of ultrathin HZO films using TEM. a, HZO thickness as a function of ALD cycles, as determined by Si atomic lattice calibration from TEM imaging. The growth rate is ~11 cycles nm^{-1}, verified across 10–50 ALD cycle films, consistent with XRR (Extended Data Fig. 2). The red error bars reflect 2σ variation. **b**, Cross-sectional ADF STEM image of 20 cycles HZO. **c**–**e**, Cross-section TEM images of ten-cycle HZO (**c**), 15-cycle HZO (**d**) and 40-cycle HZO (**e**). **f**–**h**, Wide field-of-view TEM images of ten-cycle HZO (**f**), 15-cycle HZO (**g**) and 40-cycle HZO (**h**) to provide a perspective of the heterostructure uniformity. The Si substrate is oriented along the [110] zone axis for all TEM images.

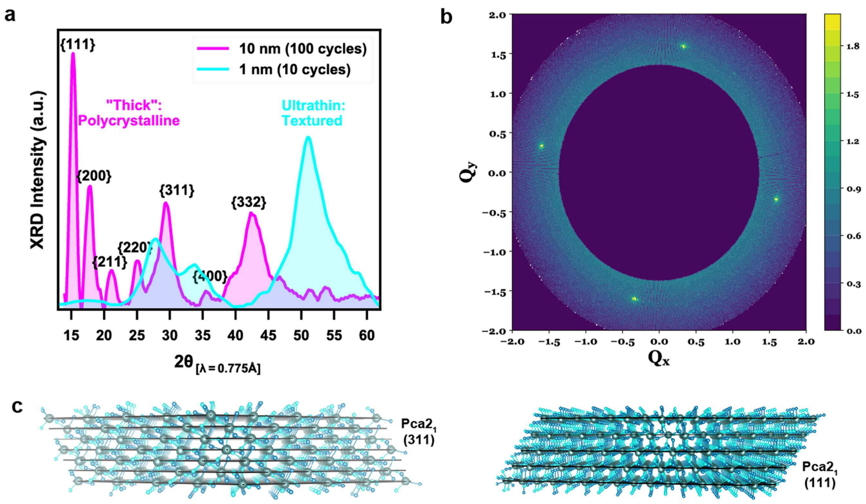

Extended Data Fig. 4 | Emergence of highly-textured films in the ultrathin regime. **a**, Synchrotron GI-XRD scans ($\lambda = 0.775$ Å) of HZO thickness series endmembers: 10-cycle and 100-cycle. The 100-cycle HZO film is indexed according to the polar orthorhombic phase $Pca2_1$. Many of the polycrystalline reflections, most notably the (111), are no longer present at an appreciable intensity in the ultrathin limit owing to the geometric constraints of one-dimensional spectra (unable to probe all reflections present in highly oriented films) (Methods). Instead tilted-geometry diffraction (pole figures) are used to access the oriented reflections. **b**, Pole figure of ten-cycle HZO, taken at a Q_x slice corresponding to the film (111) lattice spacing. The radial direction represents χ, while the azimuthal direction represents φ (0°–360° range). The presence of four intense peaks corresponding to the four (111)-projections indicate the highly textured nature of the ultrathin HZO film. The four Si (111)-projections would be expected at $\varphi = 45°$ off from the $Q_{x,y}$ principal axes at a smaller value of Q_z. **c**, Schematic of the (311) (left) and (111) (right) close-packed planes in the fluorite-structure structure. All the cation sites lie on such planes, which minimize surface energy effects because only metal-oxygen dangling bonds are present out-of-plane. We note that all schematics reflect stacking of the respective planes to a total thickness of 1 nm, although ultrathin HZO films may not exhibit such stacking throughout the film. For ten-cycle films, {311} indexing is consistent with the relevant intensity (about 30°) observed in the out-of-plane one-dimensional GI-XRD pattern (**a**), and the (111) reflections are present from the two-dimensional pole figure pattern (**b**).

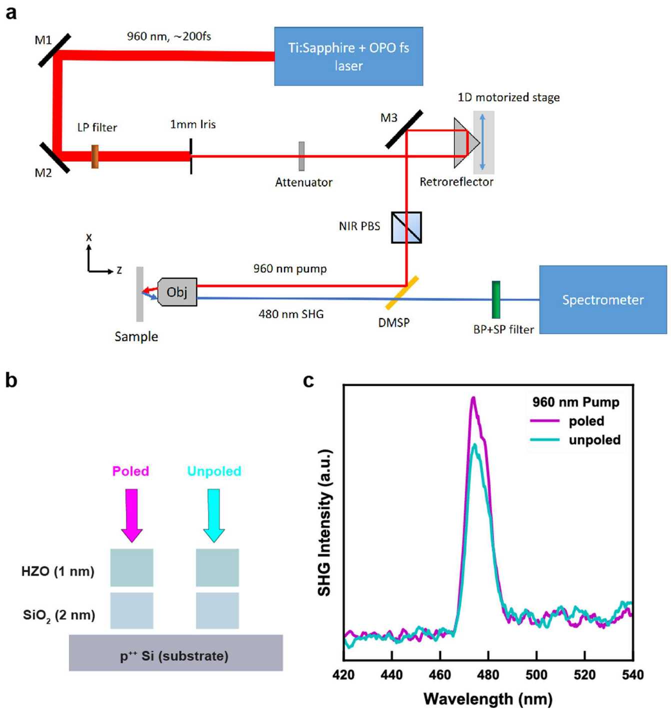

Extended Data Fig. 5 | Inversion symmetry breaking in ultrathin HZO via SHG. a, Schematic of the SHG experimental setup, using a 960-nm pump and SHG intensity detected around 480 nm under tilt incidence, which is sensitive to out-of-plane polarization (Methods). NIR, near-infrared; 1D, one-dimensional; PBS, polarized beam splitter; Obj, objective; LP, BP and SP represent long-pass, band-pass and short-pass filters; DMSP, dichroic short-pass mirror; M1, M2 and M3 refer to mirrors; OPO, optical parametric oscillator. **b**, Schematic of the ten-cycle HZO islands probed by SHG (Methods); micrometre-sized islands enabled identification of specific HZO regions either poled with an electric field (applied by a PFM tip) or left as is. For these experiments, heavily doped (10^{19} cm^{-3}) p-type Si substrates (p^{++} Si) are used to serve as the bottom electrode. **c**, SHG spectrum on a ten-cycle HZO film, comparing poled versus unpoled SHG intensity. Spontaneous polarization is demonstrated by the presence of SHG—allowed only for inversion asymmetric systems—in unpoled ten-cycle HZO. This is consistent with PFM phase contrast in unpoled HZO regions (Fig. 2c), indicating elimination of the 'wake-up' effects for ferroelectricity in ultrathin HZO. The enhanced SHG contrast in poled films—possibly due to the electric field converting a small fraction of the film to the polar phase or aligning polar domains—indicates that the mechanism behind the SHG contrast is field-tunable. This field-enhanced SHG is consistent with ferroelectric origins and would probably eliminate SHG contrast from surface effects.

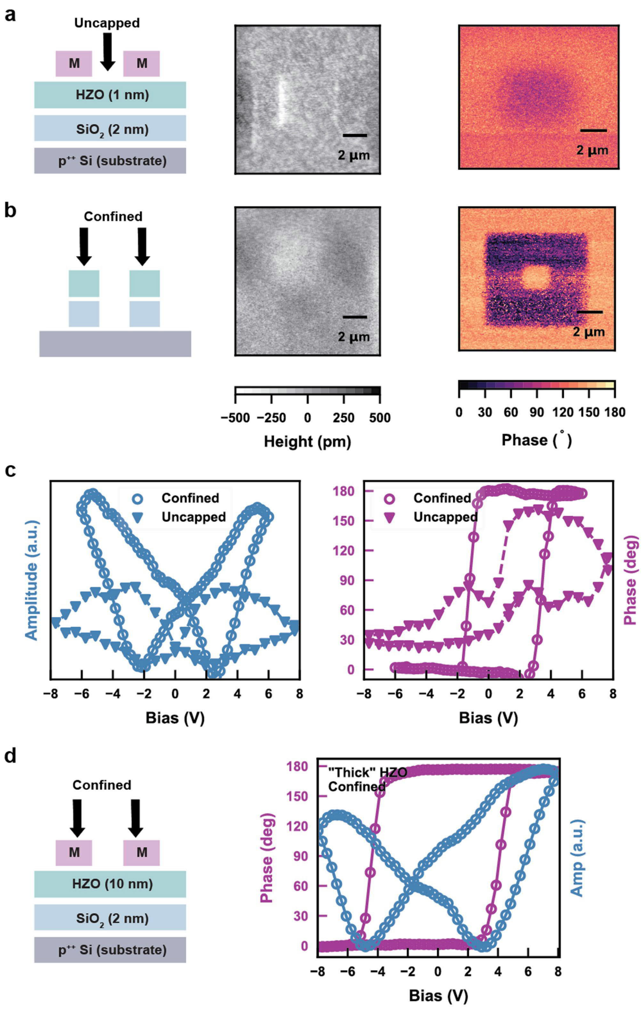

Extended Data Fig. 6 | Role of ultrathin confinement for polar phase stabilization. **a**, **b**, Schematic structure (left) probed by PFM (tip location indicated by arrows), topography (centre), and PFM phase contrast images (right) on ten-cycle HZO in a region that was uncapped (**a**) versus confined (**b**) by W (represented by 'M' for metal in the schematic) during phase annealing. Robust 180° phase contrast is only present for the confined HZO. **c**, Phase (left) and amplitude (right) switching spectroscopy loops ($V_{\mathrm{dc}} = 0$, 'OFF' state) as a function of bias voltage on ten-cycle HZO films, demonstrating the critical role of confinement during phase annealing in stabilizing ferroelectricity in ultrathin HZO. 180° phase contrast and butterfly-shaped amplitude are present only for confined HZO. Therefore, both switching-spectroscopy PFM and PFM imaging illustrate the critical role of confinement during phase annealing for stabilizing the ferroelectric phase. For the PFM images, ±7 V was applied in a 'box-in-box' poling pattern directly on the HZO surface, and switching-spectroscopy PFM loops were measured on capacitor structures (Methods). **d**, Schematic structure (left) probed by PFM (tip location indicated by arrows) and PFM phase and amplitude hysteresis loops (right) as a function of bias voltage on 100-cycle HZO in a region that was confined by W during phase annealing. Thicker 100-cycle HZO also demonstrates ferroelectric behaviour.

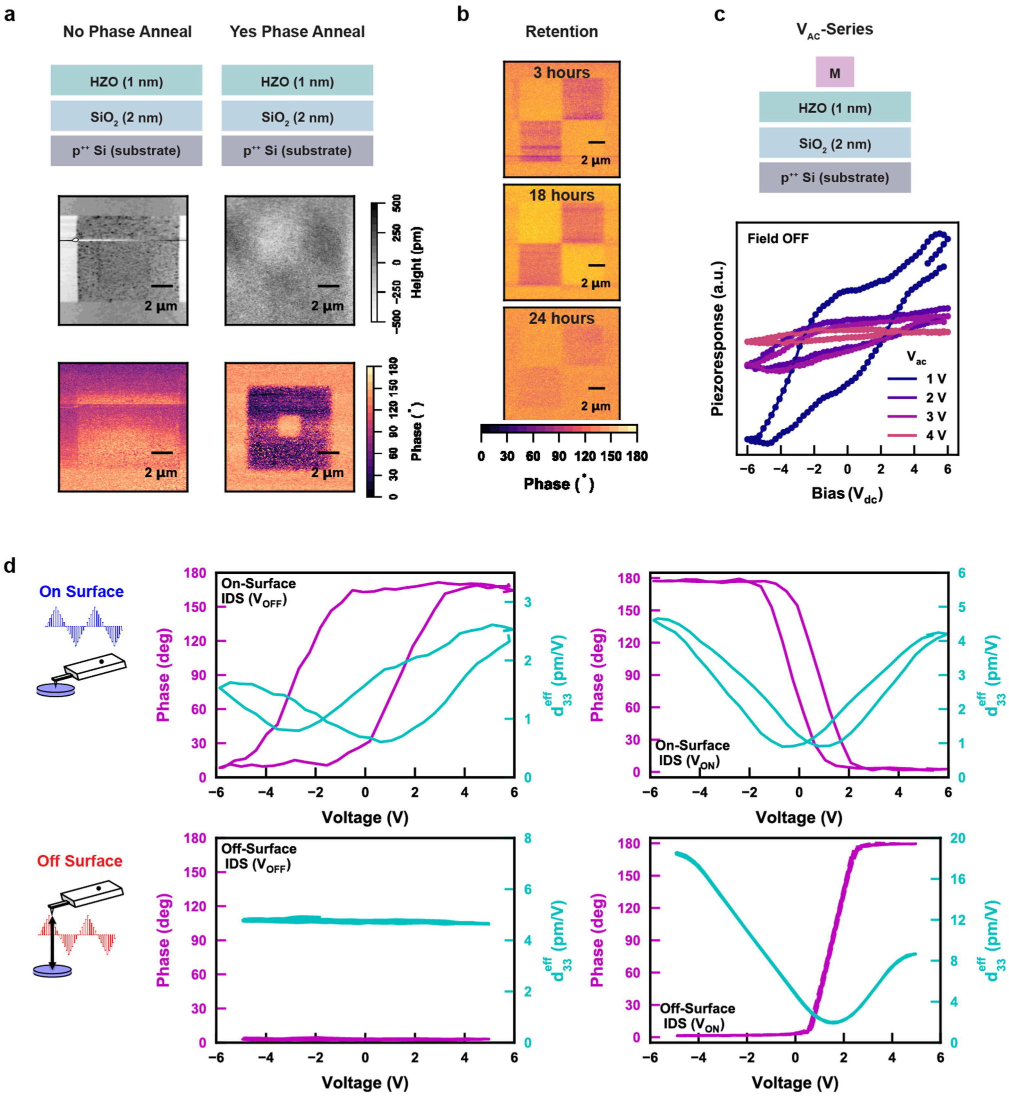

Extended Data Fig. 7 | Eliminating artefacts from scanning probe microscopy. **a**, Topography and PFM phase contrast images for ten-cycle HZO which did not (left) and did (right) undergo annealing after ALD deposition. The terraced topography in the non-annealed film indicates that the weak phase contrast is falsely caused by field-induced topographic changes. This is consistent with charge injection or ion migration, which plague amorphous HfO_2 films[25]. Phase-annealed films do not display such field-induced topographic distortions yet demonstrate much clearer phase contrast, indicating the origin of PFM phase contrast in crystalline HZO films is different than that of amorphous HZO films. In the images shown, ±7 V were applied in a 'box-in-box' poling sequence. **b**, Time-dependent PFM phase contrast images on a ten-cycle HZO film across a 24-h period. In the images shown, ±7 V was applied in the indicated checkerboard poling pattern. **c**, Collapse of the PFM loop from V_{ac}-series. Schematic capacitor structure probed by PFM (top) and piezoresponse as a function of V_{ac} in the 'OFF' ($V_{\mathrm{dc}} = 0$) state (bottom), demonstrating the collapse of the PFM loop as V_{ac} approaches the coercive voltage. This provides further confirmation of the ferroelectric origin of the PFM signal as opposed to tip bias-induced mechanisms[46]. The non-ideal shape of the piezoresponse loops, particularly at higher voltages, is probably caused by non-ferroelectric contributions from the additional dielectric SiO_2 layer through which most of the voltage is dropped (Methods). **d**, IDS switching-spectroscopy measurements on ten-cycle (1 nm) HZO, demonstrating hysteresis for the PFM tip on-surface (top) versus no hysteresis for the tip off-surface (bottom). The on-surface loops indicate 180° phase hysteresis and butterfly-shaped d_{33}, indicative of ferroelectric behaviour. IDS PFM measurements (Methods) remove the long-range electrostatics and cantilever resonance artefacts that plague typical voltage-modulated PFM switching spectroscopy[26]. This ferroelectric origin of the hysteresis is further supported by non-hysteretic off-surface loops[26], which probe electrostatic contributions.

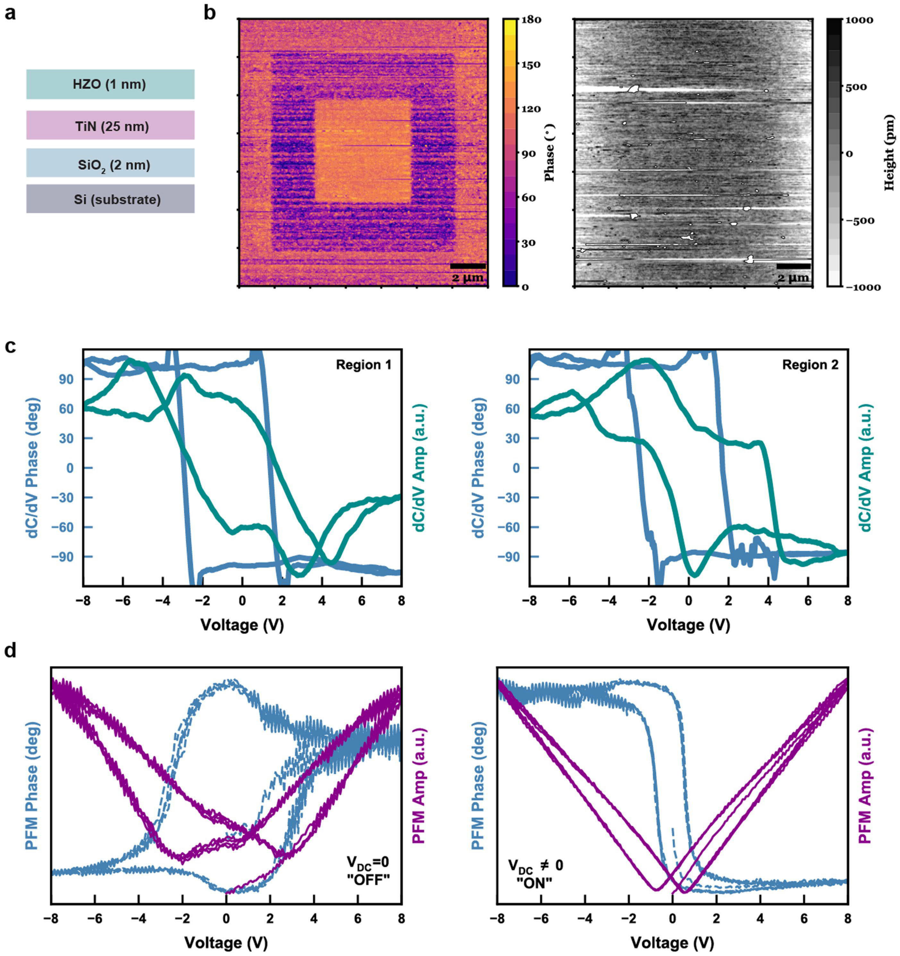

Extended Data Fig. 8 | High-frequency capacitance characterization of ultrathin HZO. a, Schematic heterostructure of ultrathin HZO on metallic TiN probed the microwave capacitance measurements to eliminate contributions from the semiconducting Si substrate. **b**, PFM phase contrast (left) and topography (right) imaging for 10 cycles HZO on TiN-buffered Si. Ultrathin ferroelectricity persists on top of metallic underlayers as well as dielectric SiO$_2$, although the topography is rougher than the films on SiO$_2$ due to the inhomogeneity introduced by the sputtered TiN. **c**, SCM d*C*–d*V* spectroscopy loops taken on multiple bare regions of an ultrathin ten-cycle HZO film, demonstrating reproducible SCM response. The square 180° phase hysteresis and d*C*/d*V* loops, which integrates into the classic butterfly-shaped capacitance–voltage plot (Fig. 2c), provides conclusive evidence of ferroelectric polarization switching beyond PFM loops (Fig. 2e, Extended Data Fig. 6). The microwave-frequency nature of the SCM enables leakage-mitigated differential capacitance measurements of ultrathin films (Methods). **d**, PFM switching-spectroscopy loops taken on the same region of the ten-cycle HZO as the SCM measurements, confirming the ferroelectric-like phase and amplitude hysteresis. We note that the SCM and PFM switching spectroscopy was done using the Asylum Cypher scanning probe microscope at Asylum Research (Methods).

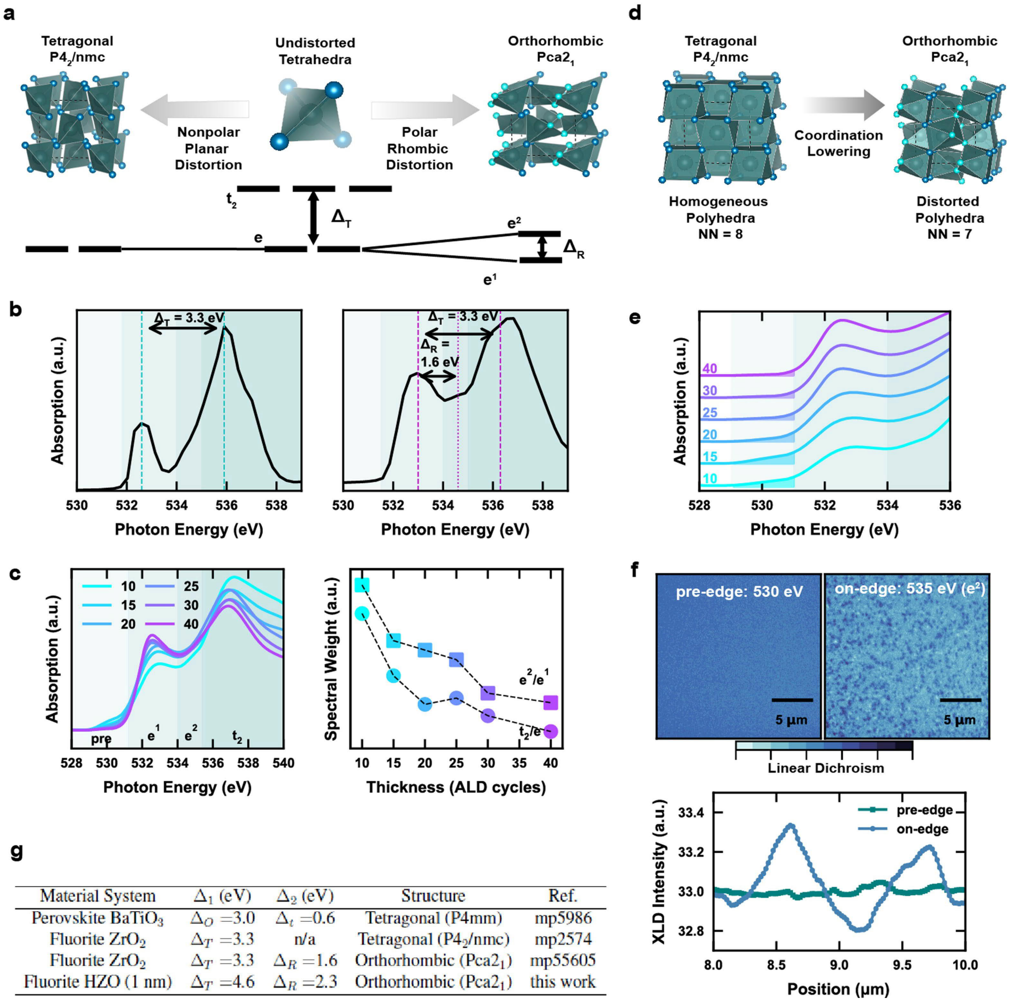

Material System	Δ_1 (eV)	Δ_2 (eV)	Structure	Ref.
Perovskite $BaTiO_3$	$\Delta_O = 3.0$	$\Delta_t = 0.6$	Tetragonal (P4mm)	mp5986
Fluorite ZrO_2	$\Delta_T = 3.3$	n/a	Tetragonal ($P4_2/nmc$)	mp2574
Fluorite ZrO_2	$\Delta_T = 3.3$	$\Delta_R = 1.6$	Orthorhombic ($Pca2_1$)	mp55605
Fluorite HZO (1 nm)	$\Delta_T = 4.6$	$\Delta_R = 2.3$	Orthorhombic ($Pca2_1$)	this work

Extended Data Fig. 9 | Ultrathin-enhanced distortions and polar signatures from spectroscopy. a, Crystal field splitting diagram for the fluorite-structure structural polymorphs; symmetry-induced *e*-splitting provides a spectroscopic signature for the polar O-phase (Methods). **b**, Delineating symmetry-split energy regimes in oxygen *K*-edge XAS. Just as convergent beam electron diffraction provides signatures to demonstrate inversion symmetry breaking[49], XAS provides spectroscopic signatures to distinguish between the nonpolar tetragonal and polar orthorhombic polymorphs (difficult to resolve from GI-XRD). Left, simulated XAS spectrum for tetragonal ZrO_2 (*P*4$_2$/*nmc*) and right, polar orthorhombic ZrO_2 (*Pca*2$_1$), both courtesy of the Materials Project[56,57]. The background colour shading denotes the symmetry-split regimes explained in the crystal field splitting diagram. **c**, Experimental XAS data on ultrathin HZO displays similar spectroscopic XAS features as the simulated polar O-phase (*Pca*2$_1$)—namely, relative e/t_2 spectral weight and splittings corresponding to tetrahedral (Δ_T) and rhombic (Δ_R) distortions. Left, XAS of the HZO thickness series at the O *K*-edge, zooming in on the *e*- and t_2-regimes. Right, O *K*-edge spectral weight trends as a function of HZO thickness. The relative spectral weights from the t_2/e and *e*-split regimes indicate enhanced tetrahedral (Δ_T) and rhombic distortions (Δ_R) in ultrathin films, respectively, consistent with C_{2v} symmetry of the polar O-phase. **d**, Schematic representation of the cation nearest-neighbour coordination dropping from NN = 8 (T-phase) to NN = 7 (polar O-phase) as the crystal symmetry is lowered. The disorder in oxygen polyhedral coordination (note the different oxygen atoms denoted by the blue and cyan atoms in the polar O-phase) manifests as spectral weight in the pre-edge regime[62]. **e**, The experimental pre-edge spectral weight as a function of thickness, indicating ultrathin-enhanced polyhedral disorder. **f**, Top: PEEM-XLD images of ten-cycle (1 nm) HZO at the O *K*-edge. Pre-edge images (left) exhibit no XLD contrast, while on-edge images (right)—at the energy corresponding to the polar-distortion split *e*-regime—demonstrate XLD contrast. This suggests that XLD is indeed sensitive to polar features in ultrathin highly textured HZO. Bottom, line profile of the XLD intensity, demonstrating substantial variations in on-edge XLD data compared to noise for pre-edge XLD. **g**, Crystal field splitting energies in HZO-related transition metal oxide systems. The material system, primary crystal electric field (Δ_1), secondary crystal electric field (Δ_2), and structure for various systems related to HZO and perovskite ferroelectrics are shown, where Δ_O, Δ_t, Δ_T and Δ_R corresponds to octahedral, tetragonal, tetrahedral, and rhombic crystal electric field (CEF), respectively. The reference crystal electric field values are taken from the Materials Project database[57] (reference codes denoted by 'mp'), and the experimental values are extracted via XAS energy-split features (**b**). The large tetrahedral (Δ_T) and rhombic (Δ_R) crystal field splitting energies present in ten-cycle HZO films are much larger than expected values for the polar fluorite-structure ZrO_2 (**b**), which highlights the enhanced distortion present in ultrathin films subject to confinement strain, and is consistent with anomalously large structural distortions extracted from diffraction (Fig. 3g).

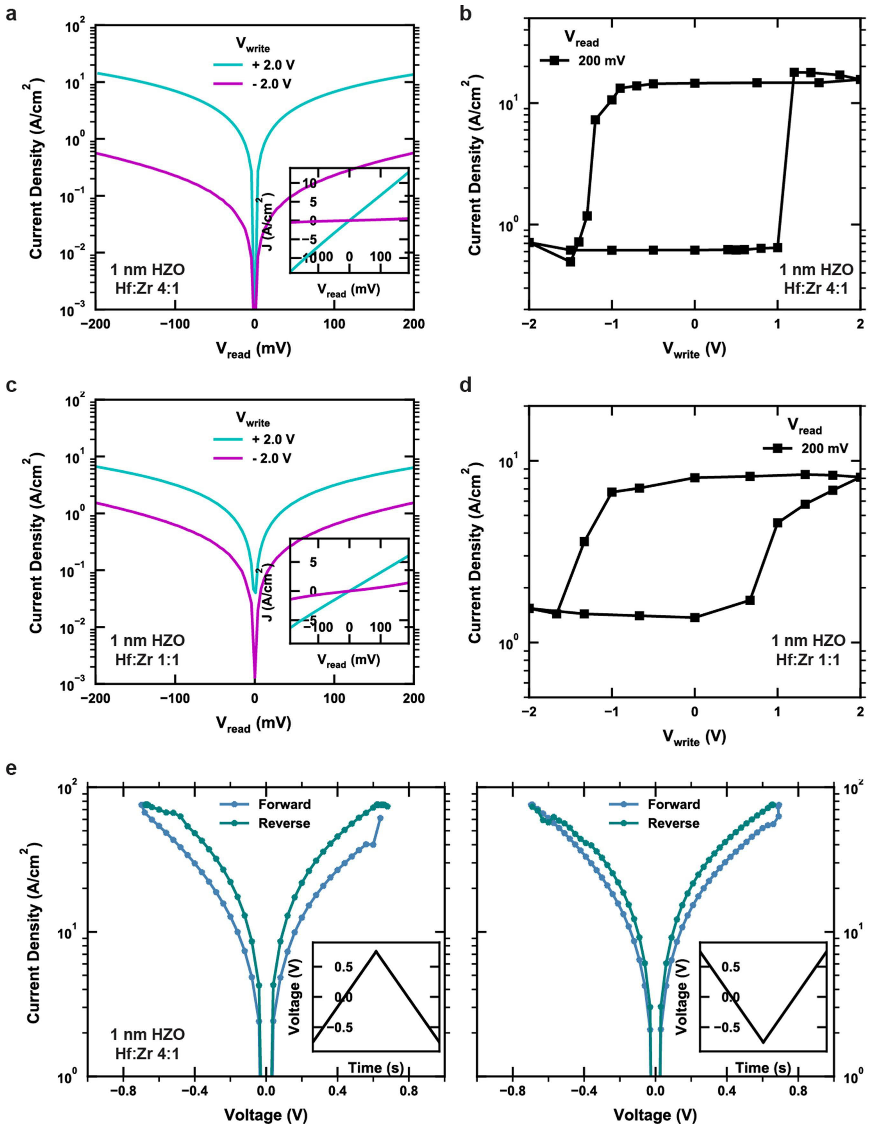

Extended Data Fig. 10 | Ultrathin HZO ferroelectric tunnel junction. a, **c**, Tunnel current–voltage characterization of Si(p^{++})/SiO$_2$(1 nm)/HZO(~1 nm)/W capacitor devices—demonstrated for ten-cycle HZO with Hf:Zr composition 4:1 (**a**) and 1:1 (**c**)—as a function of the write pulse (to set the ferroelectric polarization state). Tunnelling electroresistance behaviour is demonstrated for ±2 V write and 100 mV read. Insets, linear-scale current–voltage characteristics of the two polarization-driven current states. **b**, **d**, Tunnelling electroresistance hysteresis map as a function of write voltage (demonstrated for ten-cycle HZO with Hf:Zr composition 4:1 (**b**) and 1:1 (**d**)) measured at 200 mV read voltage. The abrupt hysteretic behaviour and saturating tunnelling electroresistance is characteristic of polarization-driven switching[67], as opposed to filamentary-based switching caused by electrochemical migration and/or oxygen vacancy motion (Methods). **e**, Current–voltage hysteresis sweeps ruling out non-polarization-driven resistive switching mechanisms (Methods). The device demonstrates current–voltage hysteresis at low voltage and voltage polarity-independent current–voltage hysteresis sense: both negative-positive-negative voltage polarity (left) and positive-negative-positive voltage polarity (right) demonstrate counter-clockwise hysteresis. Such behaviour rules out resistive switching mediated by dielectric breakdown and filamentary mechanisms[66] and is consistent with polarization-driven switching.